

# Response of Orographic Precipitation to Subsaturated Low-Level Layers

SHIZUO FU

*Department of Atmospheric and Oceanic Sciences, School of Physics, Peking University, Beijing, China*

RICHARD ROTUNNO

*National Center for Atmospheric Research, Boulder, Colorado*

HUIWEN XUE

*Department of Atmospheric and Oceanic Sciences, School of Physics, Peking University, Beijing, China*

(Manuscript received 30 April 2019, in final form 29 July 2019)

## ABSTRACT

In orographic precipitation events, there are times when subsaturated low-level layers are observed to be below saturated, nearly moist-neutral, upper-level layers. By performing a series of idealized two-dimensional simulations, this study investigates the response of orographic precipitation to subsaturated low-level layers. When the nondimensional parameter  $N_2 z_r / U$ , where  $N_2$  and  $z_r$  are, respectively, the dry Brunt–Väisälä frequency and depth of the subsaturated low-level layer, and  $U$  the cross-mountain wind speed, exceeds a critical value, the decelerated region on the upwind side of the mountain moves upwind, resulting in weak surface precipitation near the mountain peak. The critical value determined from the simulations is close to that derived from linear theory. When  $N_2 z_r / U$  is less than the critical value, increasing  $z_r$  has two competing effects: 1) the vapor-transport effect, meaning that increasing  $z_r$  decreases the amount of vapor transported to the mountain, and hence tends to decrease surface precipitation; and 2) the updraft-width effect, meaning that increasing  $z_r$  enhances flow blocking, producing a wider updraft over the upwind slope, and hence tends to increase surface precipitation. When the vapor-transport effect dominates, surface precipitation decreases with  $z_r$ . When the updraft-width effect dominates, surface precipitation increases with  $z_r$ . Increasing the maximum mountain height  $h_m$  or  $U$  generally increases surface precipitation. However, for certain combinations of  $h_m$  and  $U$ , the simulations produce lee waves, which substantially reduce surface precipitation. Finally, the response of orographic precipitation in the simulations with both liquid-phase and ice-phase microphysics is similar to that in the simulations with only liquid-phase microphysics.

## 1. Introduction

Orographic precipitation is the precipitation caused or enhanced by moist airflow past topography (Colle et al. 2013). It frequently occurs in mountainous regions, such as the east coast of East Asia (Kuo and Chen 1990; Lin et al. 2002), the west coast of North America (Galewsky and Sobel 2005; Ralph et al. 2006), and the Alpine region of Europe (Bougeault et al. 2001; Rotunno and Houze 2007). For these

regions, orographic precipitation is not only an important source of freshwater (Dettinger et al. 2011), but sometimes the cause of floods and other devastating effects (Colle and Mass 2000; Ge et al. 2010; Ralph et al. 2013).

Orographic precipitation can occur under different atmospheric stabilities. When the environmental flow is conditionally unstable, orographic lifting may trigger convection and subsequently produce surface precipitation (Miglietta and Rotunno 2009; Kirshbaum et al. 2018). Miglietta and Rotunno (2014) showed that when the cold pool produced by the convective clouds is approximately balanced by the environmental wind, the surface precipitation rate can be much larger. When the environmental flow is

---

 Denotes content that is immediately available upon publication as open access.

---

Corresponding author: Huiwen Xue, hxue@pku.edu.cn

DOI: 10.1175/JAS-D-19-0115.1

© 2019 American Meteorological Society. For information regarding reuse of this content and general copyright information, consult the [AMS Copyright Policy \(www.ametsoc.org/PUBSReuseLicenses\)](https://www.ametsoc.org/PUBSReuseLicenses).

stable, the orographic flow modification can be characterized by the nondimensional mountain height

$$M = \frac{NH}{U}, \quad (1)$$

where  $N$  is the (moist or dry) Brunt–Väisälä frequency,  $H$  the mountain height, and  $U$  the cross-mountain wind speed (Colle et al. 2013). When  $M$  is less than a critical value ( $\sim 1$ ), the flow is unblocked and goes over the mountain. When  $M$  is greater than the critical value, the flow is blocked. Compared to the unblocked situations, surface precipitation in the blocked situations generally occurs at more upwind regions (Peterson et al. 1991; Jiang 2003; Colle 2004).

Saturated, nearly moist-neutral flow is also frequently observed in orographic precipitation events (Sawyer 1956; Doswell et al. 1998; Rotunno and Ferretti 2001; Ralph et al. 2005; Rotunno and Houze 2007). By definition, a moist-neutral profile is neutral with respect to saturated adiabatic process. It is worth mentioning that such a profile is stable with respect to the dry adiabatic process. Compared to the studies of conditionally unstable flow or stable flow, there are substantially fewer studies focusing on the dynamics and precipitation associated with saturated, nearly moist-neutral flow (Colle 2004; Miglietta and Rotunno 2005, 2006, hereafter MR05, MR06, respectively; Tushaus et al. 2015). In an idealized numerical study of saturated, nearly moist-neutral flow over a ridge (MR05), it was shown that when the mountain height was less than 250 m, the whole atmosphere could remain saturated, provided that the atmosphere initially contained a small amount of cloud water. In this situation, the flow is well described by linear theory. When the mountain height was between 250 and 1500 m, an upstream-propagating disturbance desaturated the atmosphere. When the mountain height was greater than 1500 m, the whole atmosphere upwind of the mountain remained saturated while the lower troposphere downwind of the mountain became desaturated. Furthermore, MR06 showed that the inclusion of the Coriolis force suppressed the upstream-propagating disturbance.

In previous studies that used nearly moist-neutral profiles to initialize simulations, three types of relative humidity profile have been considered: 1) as mentioned above, MR05 and MR06 considered the profile to be saturated from the surface to model top; 2) Colle (2004) considered the profile to have a constant relative humidity (98%) from the surface to model top; and 3) Morales et al. (2018) considered the

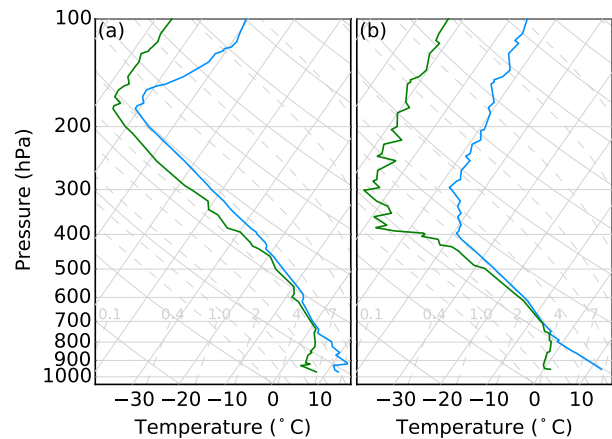


FIG. 1. (a) Sounding at 0000 UTC 18 Mar 2017 at Medford, Oregon. (b) Sounding at 0000 UTC 27 Nov 2016 at Medford, Oregon. Blue lines show the temperatures and green lines show the dewpoint temperatures.

profile to have a constant relative humidity (95%) below 4.5 km and have a decreasing relative humidity in the upper layer. As shown in those studies, these three types of profiles closely approximate some observed profiles.

Microphysics is also found to play an important role in orographic precipitation (Xue et al. 2010; Houze 2012; Stoelinga et al. 2013; Berg et al. 2017). MR06 compared liquid-only (without ice-phase microphysics) simulations to mixed-phase (with both liquid-phase and ice-phase microphysics) simulations. Their results showed that the inclusion of ice-phase microphysics substantially changed the distributions of updraft and cloud water mixing ratio. The inclusion of ice-phase microphysics generally shifted the surface precipitation farther upwind. The sensitivity study by Morales et al. (2018) showed that increasing the fall speed of snow particles also shifted the surface precipitation farther upwind.

This study investigates another type of relative humidity profile that is also observed to be associated with nearly moist-neutral flow. Unlike the three types of profiles mentioned above, this type of profile has a subsaturated, low-level layer below a saturated, upper-level layer. Figure 1a shows a sounding obtained from the west coast of North America. From 750 to 400 hPa, the profile is nearly moist neutral and saturated. Below 750 hPa, the profile is also nearly moist neutral but subsaturated. This low-level layer is stably stratified with respect to dry adiabatic process. Figure 1b shows another sounding obtained from the west coast of North America. From 800 to 400 hPa, the profile is also nearly moist neutral and saturated. Below 800 hPa, the temperature profile follows a dry

adiabatic profile, and the air is subsaturated. Such a low-level layer is neutrally stratified with respect to dry adiabatic process.

In section 2 we describe the methods used herein. Section 3 describes the mechanisms through which the subsaturated low-level layers affect the dynamics and precipitation. In sections 4 and 5, the surface precipitation of the liquid-only simulations and the mixed-phase simulations are respectively described. In section 6, a prominent phenomenon taking place in the simulations is discussed in terms of linear theory. A summary of the major findings is given in section 7.

## 2. Methods

The simulations were conducted with version 3.9.1 of the Weather Research and Forecasting (WRF) Model (Skamarock et al. 2008). The model is configured to simulate a two-dimensional (2D) flow. In the present simulations, the length and depth of the domain are 2000 and 20 km, respectively. The horizontal and vertical grid lengths are 2 and 0.25 km, respectively. A damping layer is used in the uppermost 5 km to reduce the reflection of upward-propagating gravity waves. Following MR05, second-order diffusion is used with horizontal and vertical diffusion coefficients of 3000 and  $3 \text{ m}^2 \text{ s}^{-1}$ , respectively. The lateral boundary conditions are radiative “open” conditions. The bottom boundary condition is free slip. The time step is 20 s for advection and 2 s for acoustic waves. It has been shown that this model configuration could well resolve saturated, nearly moist-neutral flow (MR05; MR06). In addition, each simulation was run for 40 h. Except for the simulations where the decelerated region on the upwind side of the mountain continuously moved upwind, the simulations reached steady state after 20 h. Thus, the results at 20 h are presented below.

Microphysics is represented with the Morrison two-moment scheme (Morrison et al. 2005, 2009), which predicts the mass mixing ratios and number concentrations of cloud droplets, rain droplets, ice crystals, snow particles, and graupel. The microphysics scheme can run in either a liquid-only scenario or a mixed-phase scenario. In the liquid-only scenario, the formation of precipitation relies on the autoconversion process, through which cloud droplets are automatically converted to rain droplets, provided that the cloud water mixing ratio is sufficiently large. The rain droplets can then grow through the accretion process (i.e., the rain droplets grow by collecting cloud droplets) and finally produce surface precipitation.

In the mixed-phase scenario, ice crystals can heterogeneously form through immersion freezing, contact freezing, and deposition nucleation. When the temperature is lower than  $-40^\circ\text{C}$ , ice crystals can also form through homogeneous freezing of cloud droplets. A complex chain of cold cloud processes can then lead to the formation of surface precipitation. In this study, we first ran the model in a liquid-only scenario. This was done in order to simplify the analysis of the dynamical processes. We then ran the model in a mixed-phase scenario to study the effect of ice-phase microphysics on the dynamics and precipitation.

The terrain was described with

$$h(x) = \frac{h_m}{1 + x^2/a^2}, \quad (2)$$

where  $h_m$  was the maximum mountain height and  $a$  the half-width of the mountain. In this study  $a = 10 \text{ km}$ . As pointed out in MR05, such a half-width is large enough for orographic effects to be detected and small enough for the Coriolis force to be neglected. Because the Coriolis force is neglected, phenomena relying on the Coriolis force, such as the barrier jet (Markowski and Richardson 2010), do not occur in our simulations. Two values of  $h_m$ , 0.7 and 1.5 km, were used here.

The initial profiles with subsaturated low-level layers were obtained by modifying the saturated, nearly moist-neutral profiles. We first discuss the calculation of the saturated, nearly moist-neutral profiles. In the liquid-only simulations, the profile is saturated with respect to water from the surface to model top. It was calculated based on the method in MR05, except that the saturation vapor pressure was given by the empirical formula (Flatau et al. 1992) that was used in the Morrison microphysics scheme. In the mixed-phase simulations, as in MR06, the profile is saturated with respect to water below the freezing level, but is saturated with respect to ice above the freezing level. The saturation vapor pressure over ice was calculated with another empirical formula from Flatau et al. (1992). Following MR05 and MR06, the moist Brunt–Väisälä frequency used in the calculation of the saturated, nearly moist-neutral profile is  $\sqrt{3} \times 10^{-3} \text{ s}^{-1}$ .

The layer below a transition height  $z_t$  was made subsaturated. This was done by setting the water vapor mixing ratio in this layer to the water vapor mixing ratio at  $z_t$ . The temperature profile was obtained using the dry Brunt–Väisälä frequency of the low-level layer  $N_2$  and the hydrostatic approximation. As discussed in

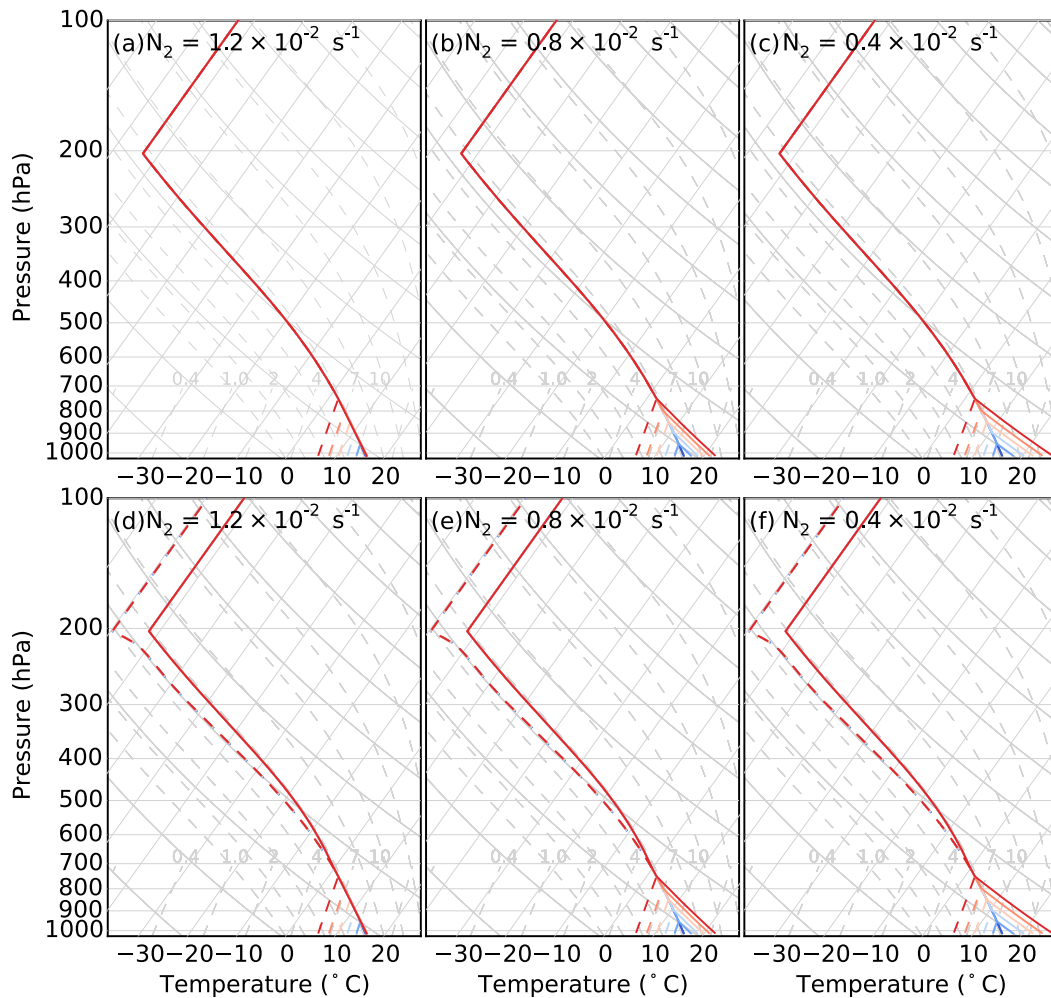


FIG. 2. Initial thermodynamic profiles (solid lines for temperature; dashed lines for dewpoint temperature) used in the liquid-only simulations with (a)  $N_2 = 1.2 \times 10^{-2} \text{ s}^{-1}$ , (b)  $N_2 = 0.8 \times 10^{-2} \text{ s}^{-1}$ , and (c)  $N_2 = 0.4 \times 10^{-2} \text{ s}^{-1}$ . (d)–(f) As (a)–(c), respectively, but for those used in the mixed-phase simulations. Profiles with progressively higher transition heights are indicated with progressively warmer colors.

section 1, the subsaturated low-level layer can be either stable or nearly neutral with respect to dry adiabatic lifting. Based on this observation, we considered three values for  $N_2$ :  $1.2 \times 10^{-2}$ ,  $0.8 \times 10^{-2}$ , and  $0.4 \times 10^{-2} \text{ s}^{-1}$ . The value of  $1.2 \times 10^{-2} \text{ s}^{-1}$  is approximately the dry Brunt–Väisälä frequency of the nearly moist-neutral profile. In addition, no  $N_2 < 0.4 \times 10^{-2} \text{ s}^{-1}$  is considered because our results indicate that the simulations with  $N_2 < 0.4 \times 10^{-2} \text{ s}^{-1}$  are similar to those of the simulations with  $N_2 = 0.4 \times 10^{-2} \text{ s}^{-1}$ . Six values of  $z_t$  were used: 0, 0.5, 1.0, 1.5, 2.0, 2.5 km. Note that the subsaturated layer is always below the freezing level ( $\sim 3$  km).

Figures 2a–c show the initial profiles of temperature and dewpoint temperature for the liquid-only simulations. Above  $z_t$ , the dewpoint temperature profile is the same as the temperature profile. Figures 2d–f show

the initial profiles for the mixed-phase simulations. Above the freezing level ( $\sim 700$  hPa), the dewpoint temperature is lower than the temperature. This is because the saturation vapor pressure over ice is lower than that over water. The saturation ratio over water decreases from 100% at the freezing level to 53% at 11.5 km. In Figs. 2d–f, the dewpoint temperatures near 200 hPa are higher than expected because the formula used to calculate the saturation vapor pressure is cut off at  $-80^\circ\text{C}$ . In all simulations, only cross-mountain wind was considered. Two wind speeds, 10 and  $20 \text{ m s}^{-1}$ , were used. These two wind speeds are commonly in studies investigating orographic precipitation (e.g., Jiang 2003; Colle 2004).

Table 1 summarizes the tested parameters and their values. The property of the subsaturated low-level

TABLE 1. Summary of tested parameters and their values.

Parameters	$h_m$ (km)	$U$ ( $\text{m s}^{-1}$ )	$N_2$ ( $10^{-2} \text{ s}^{-1}$ )	$z_t$ (km)	Microphysics
Values	0.7, 1.5	10, 20	1.2, 0.8, 0.4	0, 0.5, 1, 1.5, 2, 2.5	Liquid only, mixed phase

layer is represented with  $N_2$  and  $z_t$ . The response of orographic precipitation to  $N_2$  and  $z_t$  are investigated under different  $h_m$  and  $U$ . The effect of ice-phase microphysics is also investigated by running the simulations in different microphysical scenarios. The total number of simulations is  $2 (h_m) \times 2 (U) \times 3 (N_2) \times 6 (z_t) \times 2$  (microphysics scenario) = 144. It is worth mentioning that as long as  $h_m$ ,  $U$ , and the microphysics scheme are the same, the simulation with  $z_t = 0$  km does not change with  $N_2$ .

### 3. Mechanisms

This section presents selected liquid-only simulations with  $h_m = 0.7$  km and  $U = 10 \text{ m s}^{-1}$  to show the mechanisms through which the subsaturated low-level layer affects the dynamics and microphysics. Figure 3 shows the vertical velocities (first row), perturbation cross-mountain wind speeds (second row), cloud water mixing ratios (shadings in third row), rainwater mixing ratios (black contours in third row), autoconversion rates (fourth row), and accretion rates (fifth row) of three liquid-only simulations with  $h_m = 0.7$  km,  $U = 10 \text{ m s}^{-1}$ , and  $N_2 = 0.4 \times 10^{-2} \text{ s}^{-1}$ . In the simulation with  $z_t = 0$  km, the vertical velocity (Fig. 3a), perturbation cross-mountain wind speed (Fig. 3b), and cloud water mixing ratio (shading in Fig. 3c) are very similar to those in the simulation with the same  $h_m$  and  $U$  in MR05, although we use a different microphysics scheme and we do not add initial cloud water. The upwind propagating disturbance discussed in MR05 also appears in our simulation but has moved out of the display domain.

We now compare the simulation with  $z_t = 1$  km (Figs. 3f–j) to the simulation with  $z_t = 0$  km (Figs. 3a–e). In the simulation with  $z_t = 1$  km, Fig. 3g shows that the deceleration on the upwind side of the mountain is negligible, suggesting a negligible flow blocking. Figure 3f therefore shows that the vertical velocity in the simulation with  $z_t = 1$  km is similar to that in the simulation with  $z_t = 0$  km (cf. Fig. 3a), indicating that the dynamical response to  $z_t$  is very weak as  $z_t$  increases from 0 to 1 km. In the simulation with  $z_t = 1$  km, Fig. 3h reveals that the cloud water mixing ratio below  $z = 1$  km is much smaller than that in the simulation with  $z_t = 0$  km (cf. Fig. 3c). As  $z_t$  increases from 0 to 1 km, the humidity of the low-level layer decreases. This reduces the amount of vapor transported to the mountain. Thus,

less cloud water is formed as the low-level air ascends along the upwind slope. The smaller cloud water mixing ratio below  $z = 1$  km has two straightforward consequences. First, Fig. 3i suggests that autoconversion does not take place below  $z = 1$  km. This is because the cloud water mixing ratio is too small to trigger autoconversion. Second, Fig. 3j suggests that no accretion occurs below  $z = 1$  km. This is due to the fact that, on the one hand, the suppression of autoconversion reduces the number of rain droplets; on the other hand, there is less cloud water available to be collected when the rain droplets fall below  $z = 1$  km. Because both autoconversion and accretion are suppressed, Fig. 3h shows that the rainwater mixing ratio is much smaller in the simulation with  $z_t = 1$  km than in the simulation with  $z_t = 0$  km (cf. Fig. 3c).

The analysis above reveals the first mechanism through which the subsaturated low-level layer affects the dynamics and microphysics. Briefly, when the dynamical effect is negligible, such as the simulations discussed above, increasing  $z_t$  decreases the amount of vapor transported to the mountain, suppressing both autoconversion and accretion, and finally leads to a smaller rainwater mixing ratio. This effect is termed the “vapor-transport effect.” When  $z_t$  is further increased to 2 km (Figs. 3k–o), Fig. 3k suggests that the dynamical effect is still negligible. In this situation, the vapor-transport effect further reduces the rainwater mixing ratio (cf. Figs. 3m,h).

Figure 4 shows the results of three liquid-only simulations with  $h_m = 0.7$  km,  $U = 10 \text{ m s}^{-1}$ , and  $N_2 = 1.2 \times 10^{-2} \text{ s}^{-1}$ . In the simulation with  $z_t = 1$  km, the low-level layer is initially very stable. Although Fig. 4h indicates that condensation occurs as the low-level air ascends along the upwind slope, the condensation rate is very small. The release of latent heat does not substantially reduce the stability of the low-level layer. Figure 4g reveals a prominent deceleration on the upwind side of the mountain, indicating a strong flow blocking. The blocking effectively extends the mountain upwind. The updraft over the upwind slope therefore becomes much wider than that in the simulation with  $z_t = 0$  km (cf. Figs. 4f,a). In the simulation with  $z_t = 1$  km, Fig. 4g shows that the full cross-mountain wind (which is the sum of the perturbation cross-mountain wind and  $U$ ) between  $z = 1$  and 4 km is only slightly faster than that in the simulation with  $z_t = 0$  km (cf. Fig. 4b). In this situation, the wider updraft in the simulation with  $z_t = 1$  km

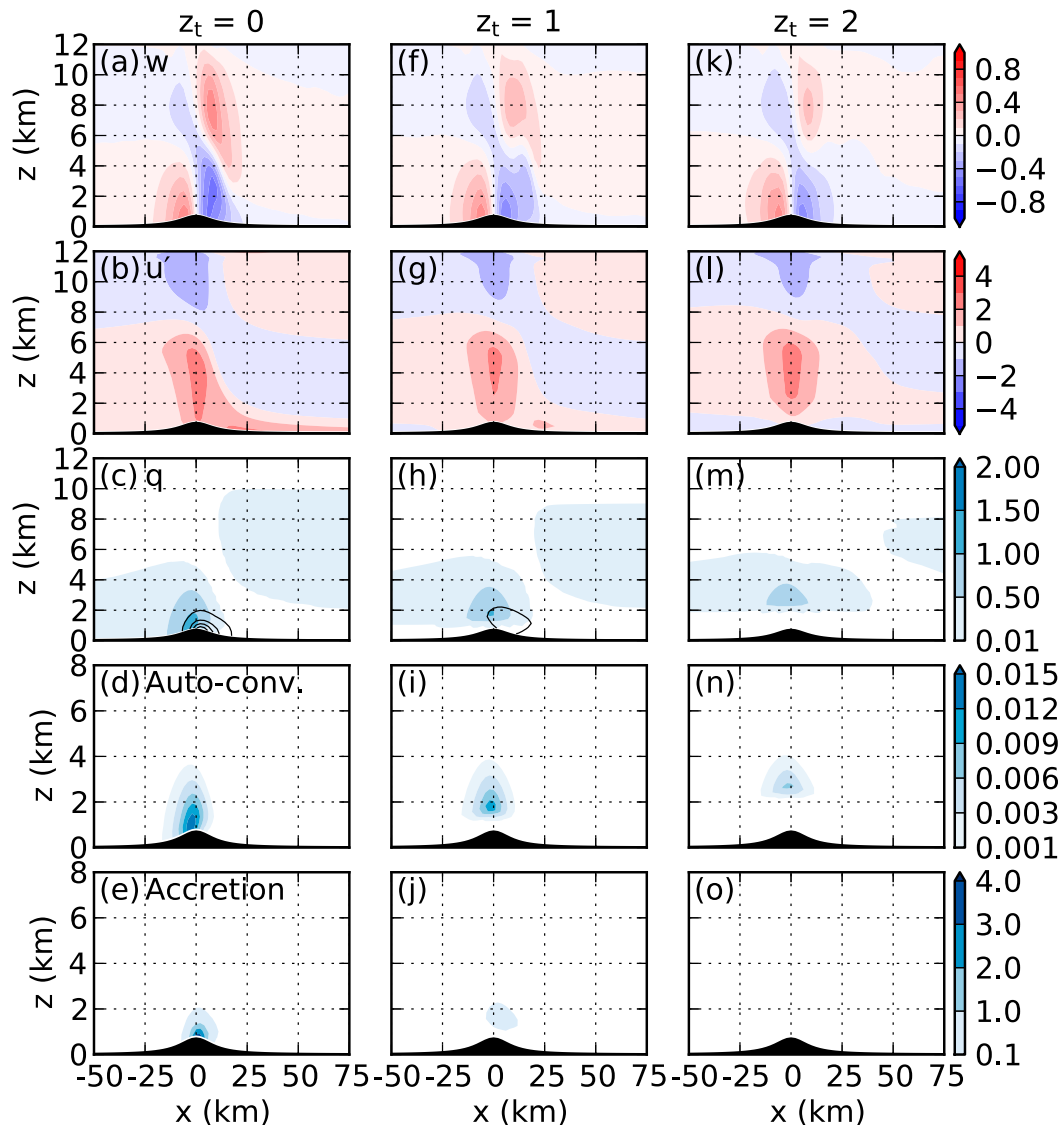


FIG. 3. Results at  $t = 20$  h of three liquid-only simulations with  $h_m = 0.7$  km,  $U = 10$  m s $^{-1}$ , and  $N_2 = 0.4 \times 10^{-2}$  s $^{-1}$ ; values of  $z_t$  (km) are shown above each column. Rows show (a),(f),(k) the vertical velocities (m s $^{-1}$ ); (b),(g),(l) the perturbation cross-mountain wind speeds (m s $^{-1}$ ); (c),(h),(m) the cloud water mixing ratios (g kg $^{-1}$ ; shaded) and rainwater mixing ratios (g kg $^{-1}$ ; black contours starting from 0.01 g kg $^{-1}$  with a contour interval of 0.05 g kg $^{-1}$ ); (d),(i),(n) the autoconversion rates (g kg $^{-1}$  h $^{-1}$ ); and (e),(j),(o) the accretion rates (g kg $^{-1}$  h $^{-1}$ ). We note that the ordinate ranges of the bottom two rows are different from those of the first three rows.

means that the parcels between  $z = 1$  and 4 km experience ascent for a longer time, and hence rise to higher elevations. Thus, condensation occurs higher up and farther upwind in the simulation with  $z_t = 1$  km than in the simulation with  $z_t = 0$  km (cf. Figs. 4h,c). As a result, Fig. 4i shows that autoconversion takes place higher up and farther upwind in the simulation with  $z_t = 1$  km (cf. Fig. 4d). Figure 4j further suggests that accretion occurs over a wider region and has a larger maximum value in the simulation with  $z_t = 1$  km (cf. Fig. 4e), indicating that more cloud water is collected by

the falling rain droplets, and is consequently converted to rainwater. As a result, Fig. 4h shows that the rainwater mixing ratio in the simulation with  $z_t = 1$  km is larger than that in the simulation with  $z_t = 0$  km (cf. Fig. 4c).

The analysis above reveals the second mechanism through which the subsaturated low-level layer affects the dynamics and microphysics. Increasing  $z_t$  widens the updraft, enhancing the conversion from cloud water to rainwater, and consequently producing a larger rainwater mixing ratio. This effect is termed the

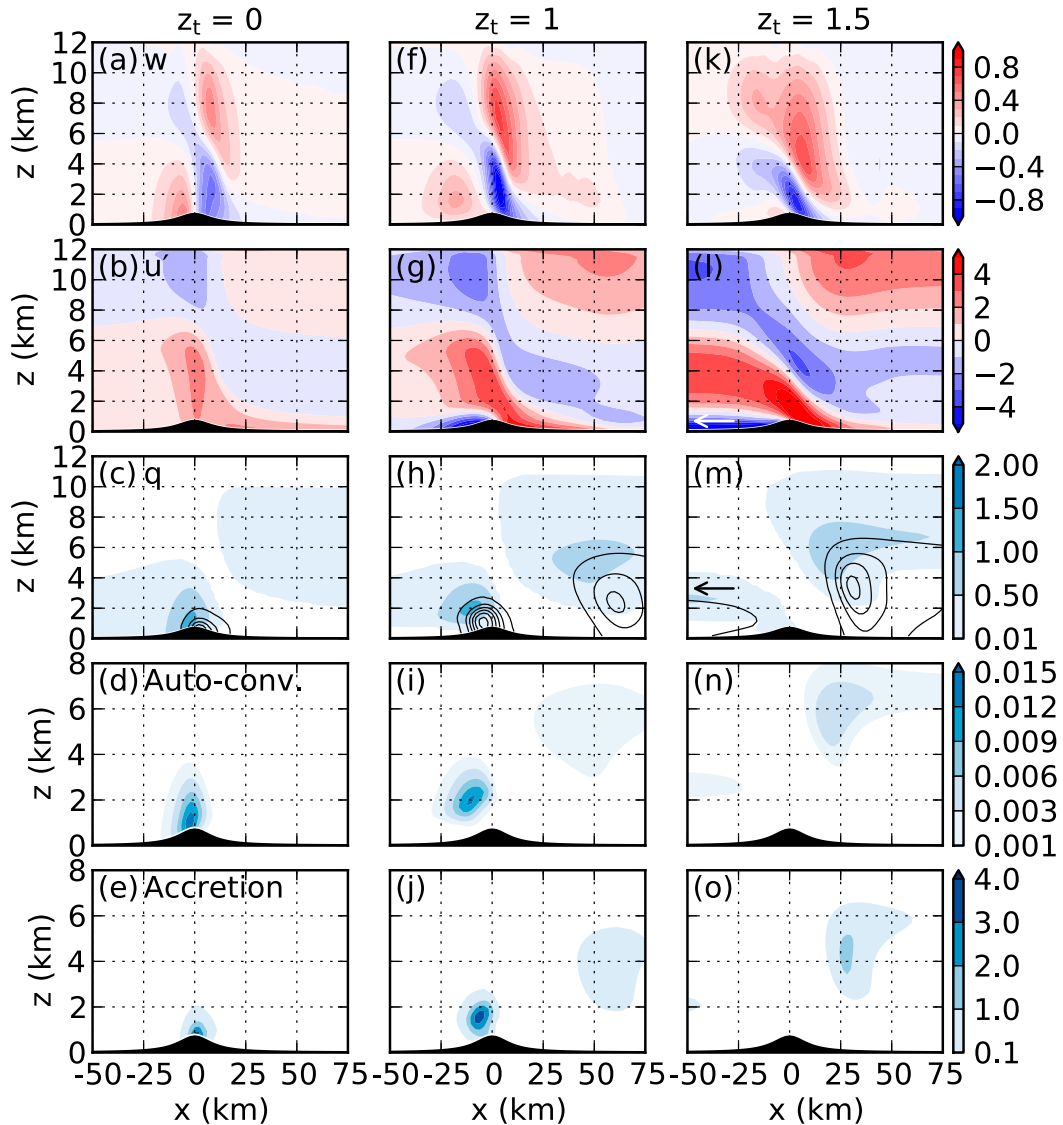


FIG. 4. As in Fig. 3, but for three liquid-only simulations with  $h_m = 0.7$  km,  $U = 10$  m s<sup>-1</sup>, and  $N_2 = 1.2 \times 10^{-2}$  s<sup>-1</sup>. The arrows in (l)–(m) show the direction of movement.

“updraft-width effect.” We note that the vapor-transport effect is also active in the examples discussed above ( $h_m = 0.7$  km,  $U = 10$  m s<sup>-1</sup>,  $N_2 = 1.2 \times 10^{-2}$  s<sup>-1</sup>, and  $z_t$  increases from 0 to 1 km); however, it is much weaker than the updraft-width effect.

In the simulation with  $z_t = 1.5$  km (Figs. 4k–o), initially there is no condensation occurring below the maximum mountain height (not shown). The low-level layer is therefore stable. Figure 4l reveals a remarkable deceleration on the upwind side of the mountain, indicating a strong flow blocking. Unlike the simulations with  $z_t < 1.5$  km, where the decelerated region is stationary (cf. Fig. 4g); in the simulation with  $z_t = 1.5$  km, the decelerated region moves upwind. This upwind

movement forces the deep updraft to move away from the mountain peak. At  $t = 20$  h, Fig. 4k shows that the updraft near the mountain peak is much shallower and weaker than that in the simulations with  $z_t < 1.5$  km. On the upwind side of the mountain, Fig. 4m suggests that the cloud water mixing ratio is very small. Figure 4n thus suggests that the autoconversion rate is much smaller than that in the simulations with  $z_t < 1.5$  km. Figure 4o reveals that the accretion rate is almost negligible. Thus, very little rainwater forms on the upwind side of the mountain (Fig. 4m).

The analysis above reveals the third mechanism through which the subsaturated low-level layer affects the dynamics and microphysics. When  $z_t$  is greater

than a certain value, the decelerated region on the upwind side of the mountain moves upwind, resulting in a very shallow and weak updraft near the mountain peak. As a consequence, the rainwater mixing ratio near the mountain peak becomes very small. The upwind movement of the decelerated region will be further discussed in section 6.

#### 4. Surface precipitation of liquid-only simulations

In this section, we present the response of surface precipitation to the subsaturated low-level layers in the liquid-only simulations. For most simulations, we simply use the three mechanisms identified in section 3 to explain the variation of surface precipitation with  $z_t$ . For the other simulations, the details are presented because they are more complicated.

a.  $h_m = 0.7 \text{ km}$  and  $U = 10 \text{ m s}^{-1}$

Figure 5a shows the rain-rate distributions in the simulations with  $h_m = 0.7 \text{ km}$ ,  $U = 10 \text{ m s}^{-1}$ , and  $N_2 = 1.2 \times 10^{-2} \text{ s}^{-1}$ . Note that rain rate in this study specifically refers to the rain rate on the surface. When  $z_t$  increases from 0 to 1 km, the updraft-width effect dominates the vapor-transport effect. Thus, the rain rate increases with  $z_t$  (Fig. 5a). Figure 5a also reveals that the precipitation in the simulation with  $z_t = 1 \text{ km}$  is located farther upwind compared to that in the simulation with  $z_t = 0 \text{ km}$ , consistent with the fact that autoconversion occurs farther upwind in the simulation with  $z_t = 1 \text{ km}$  (cf. Figs. 4i,d). In the simulations with  $z_t \geq 1.5 \text{ km}$ , the rain rate near the mountain peak is negligible, consistent with the negligible rainwater mixing ratio near the mountain (Fig. 4m). However, Fig. 5a indicates that surface precipitation forms on the downwind side of the mountain in the simulations with  $z_t \geq 1.5 \text{ km}$ . On the downwind side of the mountain, Fig. 4k shows that the updraft aloft is quite strong. This produces a sufficiently large cloud water mixing ratio aloft (Fig. 4m), leading to the formation of rainwater (Fig. 4m). In addition, due to the vapor-transport effect, Fig. 5a shows that the rain rate on the downwind side of the mountain decreases with  $z_t$ .

Figure 5b shows the rain-rate distributions in the simulations with a smaller  $N_2 = 0.8 \times 10^{-2} \text{ s}^{-1}$ . Due to the smaller  $N_2$ , the flow blocking in the simulations with  $N_2 = 0.8 \times 10^{-2} \text{ s}^{-1}$  is generally weaker than that in the simulations with  $N_2 = 1.2 \times 10^{-2} \text{ s}^{-1}$ . In the simulations with  $z_t \leq 1.5 \text{ km}$ , the updraft-width effect is weaker than the vapor-transport effect, Fig. 5b therefore reveals a decrease of rain rate with  $z_t$ . In the simulations with  $z_t \geq 2 \text{ km}$ , the decelerated region moves

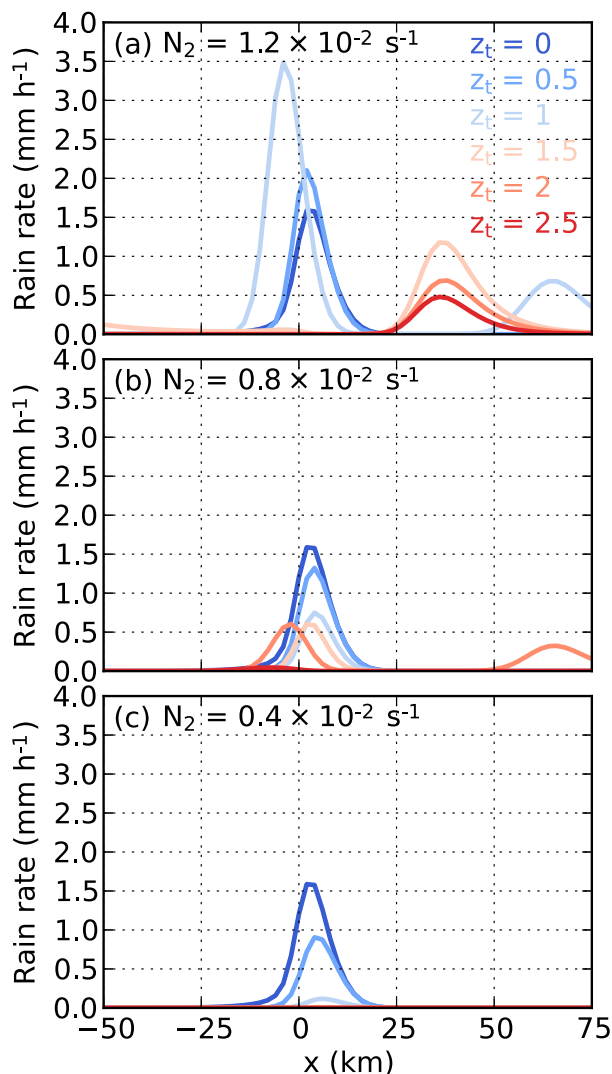


FIG. 5. The surface rain rate as a function of distance from the mountain peak (at  $x = 0$ ) at  $t = 20 \text{ h}$  of the liquid-only simulations with  $h_m = 0.7 \text{ km}$  and  $U = 10 \text{ m s}^{-1}$ . (a)  $N_2 = 1.2 \times 10^{-2}$ , (b)  $N_2 = 0.8 \times 10^{-2}$ , and (c)  $N_2 = 0.4 \times 10^{-2} \text{ s}^{-1}$ . Simulations with different  $z_t$  (km) are shown with different colors.

upwind (not shown). However, in the simulation with  $z_t = 2 \text{ km}$ , the upwind movement occurs very slowly; at  $t = 20 \text{ h}$ , the updraft is still near the mountain peak and becomes much wider than that in the simulation with  $z_t = 1.5 \text{ km}$  (not shown). The updraft-width effect counteracts the vapor-transport effect. Therefore, Fig. 5b shows that the surface precipitation in the simulation with  $z_t = 2 \text{ km}$  is almost the same as that in the simulation with  $z_t = 1.5 \text{ km}$ , except that the surface precipitation is shifted upwind. In the simulation with  $z_t = 2 \text{ km}$ , surface precipitation also forms on the downwind side of the mountain (Fig. 5b). In the simulation with  $z_t = 2.5 \text{ km}$ , the decelerated region rapidly

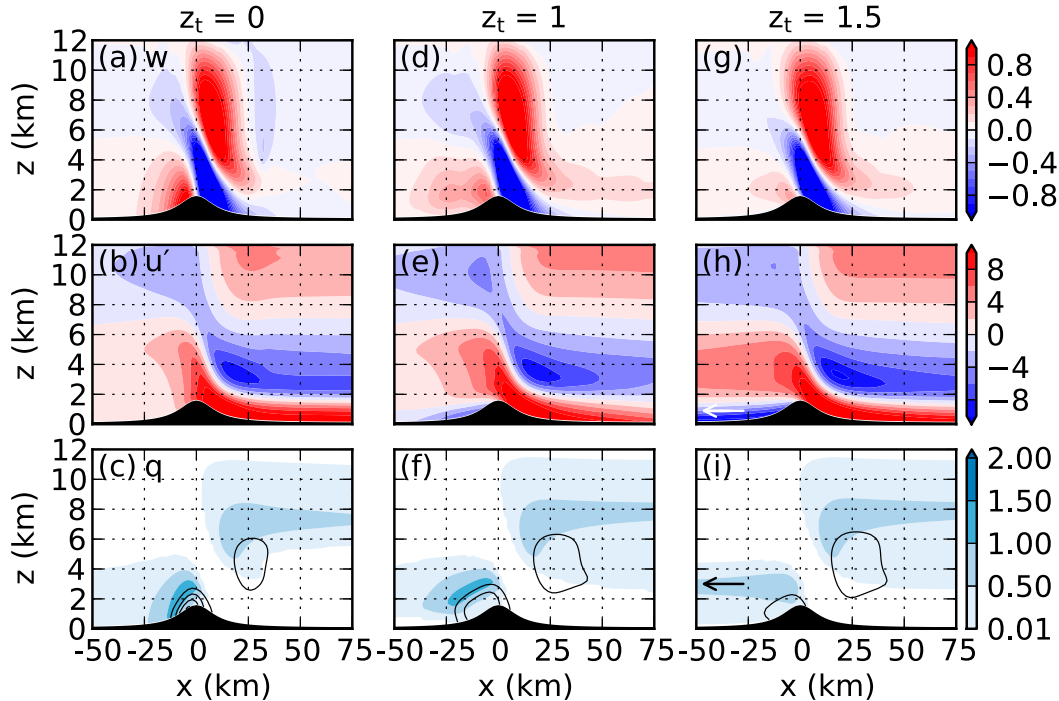


FIG. 6. Results at  $t = 20$  h of three liquid-only simulations with  $h_m = 1.5$  km,  $U = 10$  m s $^{-1}$ , and  $N_2 = 1.2 \times 10^{-2}$  s $^{-1}$ ; values of  $z_t$  (km) are shown above each column. Rows show (a),(d),(g) the vertical velocity (m s $^{-1}$ ); (b),(e),(h) the perturbation cross-mountain wind (m s $^{-1}$ ); and (c),(f),(i) the cloud water mixing ratio (g kg $^{-1}$ ; shaded) and rainwater mixing ratio (g kg $^{-1}$ ; black contours starting from 0.1 g kg $^{-1}$  with a contour interval of 0.2 g kg $^{-1}$ ). The arrows in (h) and (i) show the direction of propagation.

moves upwind. Thus, Fig. 5b suggests that very little surface precipitation forms near the mountain peak.

In the simulations with an even smaller  $N_2 = 0.4 \times 10^{-2}$  s $^{-1}$ , the flow blocking is even weaker (e.g., Figs. 3b,g,l). As discussed in section 3, the updraft-width effect is negligible, while the vapor-transport effect is active. Figure 5c thus indicates a decrease of rain rate with  $z_t$ . In all the simulations with  $N_2 = 0.4 \times 10^{-2}$  s $^{-1}$ , the decelerated regions do not move upwind.

#### b. $h_m = 1.5$ km and $U = 10$ m s $^{-1}$

Figure 6 shows the results of three liquid-only simulations with  $h_m = 1.5$  km,  $U = 10$  m s $^{-1}$ , and  $N_2 = 1.2 \times 10^{-2}$  s $^{-1}$ . In the simulation with  $z_t = 0$  km, the vertical velocity (Fig. 6a) and perturbation cross-mountain wind speed (Fig. 6b) are very similar to those in the simulation with  $h_m = 0.7$  km (Figs. 3a,b), except that the magnitudes are nearly doubled. This doubling is consistent with linear theory, where the patterns of vertical velocity and perturbation cross-mountain wind speed do not change with  $h_m$  but their magnitudes proportionally increase with  $h_m$  (Lin 2007, 109–112). However, the microphysical responses are more complicated. In the simulation with  $h_m = 0.7$  km,

autoconversion mainly occurs below  $z = 4$  km (Fig. 3d), and the accretion rate is very small (Fig. 3e), so only a small portion of cloud water is converted to rainwater. In the simulation with  $h_m = 1.5$  km, Fig. 6c shows that the higher mountain produces a larger cloud water mixing ratio (cf. Fig. 3c). Autoconversion is initiated higher up (not shown). The converted rain droplets hence collect much more cloud water (not shown), leading to a much larger rainwater mixing ratio (cf. Figs. 6c and 3c). For the simulations with  $z_t = 0$  km, Fig. 7a shows that the rain rate in the simulation with  $h_m = 1.5$  km is much larger than that in the simulation with  $h_m = 0.7$  km (cf. Fig. 5a). On the downwind side of the mountain, Fig. 6a shows that the updraft aloft is very strong, leading to the formation of cloud water (Fig. 6c) and consequently surface precipitation (Fig. 7a).

Figure 7a shows the effect of varying  $z_t$  on the rain-rate distribution in the simulations with  $h_m = 1.5$  km,  $U = 10$  m s $^{-1}$ , and  $N_2 = 1.2 \times 10^{-2}$  s $^{-1}$ . As  $z_t$  increases from 0 to 0.5 km, the updraft-width effect nearly counteracts the vapor-transport effect. Figure 7a thus shows similar rain rates in these two simulations. As  $z_t$  further increases to 1 km, the situation becomes slightly more complicated. Figure 6e shows that flow blocking is

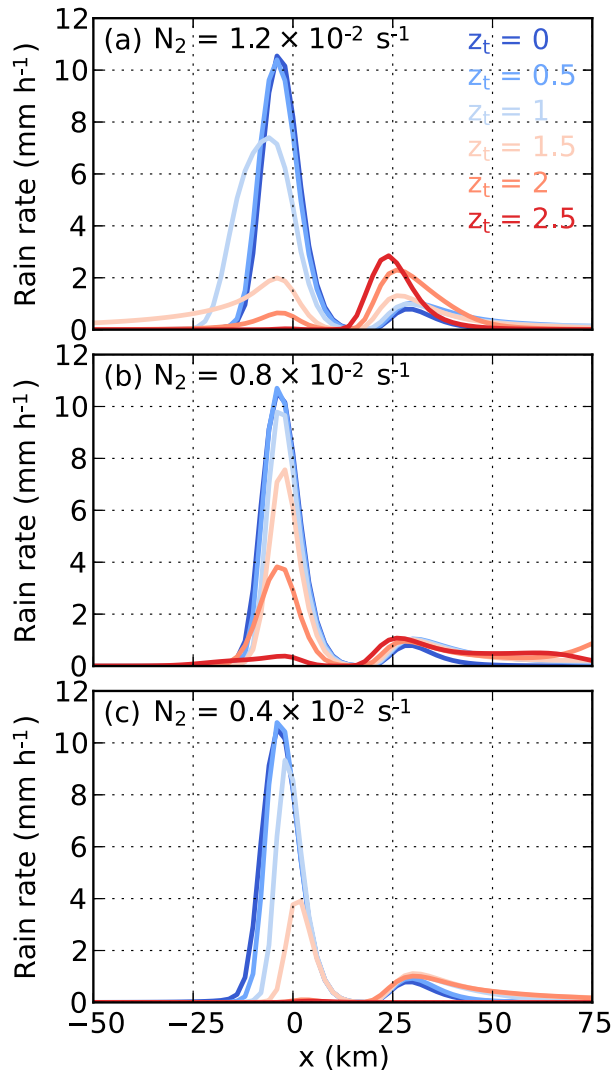


FIG. 7. As in Fig. 5, but for the liquid-only simulations with  $h_m = 1.5$  km and  $U = 10$  m s $^{-1}$ .

strong in the simulation with  $z_t = 1$  km. Compared with the simulation with  $z_t = 0$  km, the simulation with  $z_t = 1$  km has a wider but weaker updraft over the upwind slope (cf. Figs. 6d,a). Consequently, rainwater forms over a wider region but has a smaller maximum value (cf. Figs. 6f,c). Figure 7a hence indicates that the rain rate is spread over a wider region but has a smaller maximum value. In the simulations with  $z_t \geq 1.5$  km, the decelerated region moves upwind (e.g., Figs. 6h,i). At  $t = 20$  h, the updraft over the upwind slope becomes very weak (e.g., Fig. 6g). Nevertheless, Fig. 6i suggests that cloud water still forms near the mountain peak, and is finally converted to rainwater. Figure 7a therefore shows that surface precipitation forms near the mountain peak. In the simulations with  $z_t \geq 1.5$  km, the updraft-width effect

does not take effect while the vapor-transport effect is still active. Figure 7a thus reveals a decrease of rain rate with  $z_t$ . On the downwind side of the mountain, increasing  $z_t$  generally increases the width of the updraft aloft (cf. Figs. 6a,d,g). Rain rate therefore increases with  $z_t$  (Fig. 7a).

In the simulations with a smaller  $N_2 = 0.8 \times 10^{-2} \text{ s}^{-1}$  (not shown), the flow blocking is generally weaker than that in the simulations with  $N_2 = 1.2 \times 10^{-2} \text{ s}^{-1}$ . With reduced blocking, the updraft-width effect is generally weaker than the vapor-transport effect. Figure 7b therefore shows that the rain rate decreases as  $z_t$  increases from 0 to 2 km. In the simulation with  $z_t = 2.5$  km, the decelerated region moves upwind, resulting in negligible precipitation near the mountain peak (Fig. 7b). In all the simulations with  $N_2 = 0.8 \times 10^{-2} \text{ s}^{-1}$ , Fig. 7b shows that surface precipitation occurs on the downwind side of the mountain. In addition, when  $z_t \geq 0.5$  km, surface precipitation spreads over a wide region. For an even smaller  $N_2 = 0.4 \times 10^{-2} \text{ s}^{-1}$  (not shown), the flow blocking is even weaker, and the updraft-width effect becomes even weaker than the vapor-transport effect. Consequently, rain rate monotonically decreases with  $z_t$  (Fig. 7c). In addition, surface precipitation also occurs on the downwind side of the mountain (Fig. 7c). In all simulations with  $N_2 = 0.4 \times 10^{-2} \text{ s}^{-1}$ , the decelerated regions do not move upwind (not shown).

c.  $h_m = 1.5$  km and  $U = 20$  m s $^{-1}$

Figure 8 shows the results of three liquid-only simulations with  $h_m = 1.5$  km,  $U = 20$  m s $^{-1}$ , and  $N_2 = 1.2 \times 10^{-2} \text{ s}^{-1}$ . Figure 8a shows that in the simulation with  $z_t = 0$  km, the updraft over the upwind slope is approximately twice as deep as that in the simulation with  $U = 10$  m s $^{-1}$  (cf. Fig. 6a). This doubling is also consistent with linear theory, where the vertical wavelength is proportional to  $U$  (Lin 2007, 109–112). The much deeper updraft produces a much deeper cloud (cf. Figs. 8c and 6c), which subsequently produces a larger rainwater mixing ratio. For the simulations with  $z_t = 0$  km, Fig. 9a shows that the rain rate in the simulation with  $U = 20$  m s $^{-1}$  is much larger than that in the simulation with  $U = 10$  m s $^{-1}$  (cf. Fig. 7a).

Figure 9a shows the rain-rate distributions for the simulations with  $h_m = 1.5$  km,  $U = 20$  m s $^{-1}$ , and  $N_2 = 1.2 \times 10^{-2} \text{ s}^{-1}$ . Increasing  $z_t$  from 0 to 1.5 km does not significantly change the rain rate, because the updraft-width effect nearly counteracts the vapor-transport effect in these simulations. However, Fig. 9a indicates that the rain rate in the simulation with  $z_t = 2$  km is larger than that in the simulations with  $z_t = 1.5$  km. In the simulation with  $z_t = 2$  km, Fig. 8e suggests a strong

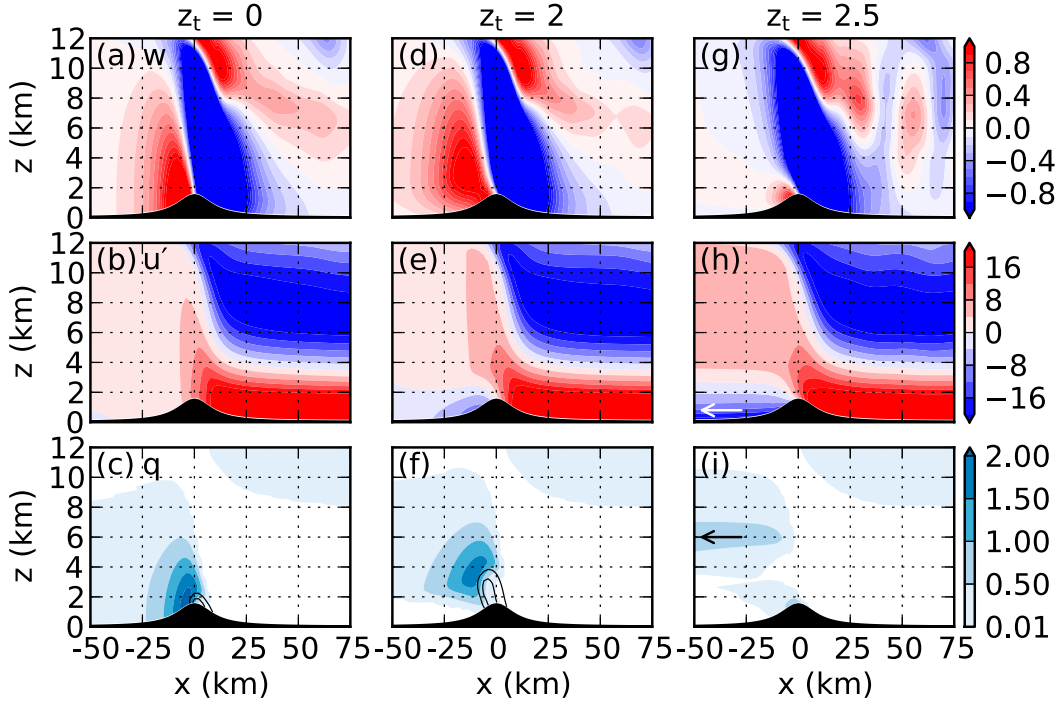


FIG. 8. Results at  $t = 20$  h of three liquid-only simulations with  $h_m = 1.5$  km,  $U = 20$  m s $^{-1}$ , and  $N_2 = 1.2 \times 10^{-2}$  s $^{-1}$ ; values of  $z_t$  (km) are shown above each column. Rows show (a),(d),(g) the vertical velocity (m s $^{-1}$ ); (b),(e),(h) the perturbation cross-mountain wind (m s $^{-1}$ ); and (c),(f),(i) the cloud water mixing ratio (g kg $^{-1}$ ; shaded) and rainwater mixing ratio (g kg $^{-1}$ ; black contours starting from 0.5 g kg $^{-1}$  with a contour interval of 0.5 g kg $^{-1}$ ). The arrows in (h) and (i) show the direction of propagation.

flow blocking. Figure 8d therefore indicates that the updraft over the upwind slope becomes very wide. As  $z_t$  increases from 1.5 to 2 km, the updraft-width effect surpasses the vapor-transport effect, leading to an increase of rain rate. Figure 9a also shows that the rain rate near the mountain peak is very small in the simulation with  $z_t = 2.5$  km. This is because the decelerated region moves upwind in this simulation (Figs. 8g–i).

In the simulations with a smaller  $N_2 = 0.8 \times 10^{-2}$  s $^{-1}$  (not shown), the flow blocking is generally weaker than those in the simulations with  $N_2 = 1.2 \times 10^{-2}$  s $^{-1}$ . In these simulations, the updraft-width effect is generally weaker than the vapor-transport effect. Consequently, Fig. 9b shows that the rain rate decreases monotonically with  $z_t$ . The simulations with  $N_2 = 0.4 \times 10^{-2}$  s $^{-1}$  are similar to the simulations with  $N_2 = 0.8 \times 10^{-2}$  s $^{-1}$ , except that the rain rate decreases with  $z_t$  even faster (Fig. 9c). In all simulations with  $N_2 = 0.8 \times 10^{-2}$  and  $0.4 \times 10^{-2}$  s $^{-1}$ , the decelerated regions do not move upwind (not shown).

d.  $h_m = 0.7$  km and  $U = 20$  m s $^{-1}$

Figure 10 shows the results of three liquid-only simulations with  $h_m = 0.7$  km,  $U = 20$  m s $^{-1}$ , and

$N_2 = 1.2 \times 10^{-2}$  s $^{-1}$ . The vertical velocity suggests that lee waves form in these simulations (Figs. 10a,d,g). In a two-layer atmosphere, the condition for lee waves is (Scorer 1949; Lehner et al. 2016)

$$l_l^2 - l_u^2 > \frac{\pi^2}{4z_l^2}, \quad (3)$$

where  $z_l$  is the thickness of the lower layer, and  $l_l$  and  $l_u$  are, respectively, the Scorer parameters of the lower and the upper layers, and

$$l_i^2 = \frac{N_i^2}{U_i^2} - \frac{1}{U_i} \frac{d^2 U_i}{dz^2}, \quad (4)$$

where  $i$  refers to  $l$  or  $u$ , and  $N_i$  and  $U_i$  are, respectively, the Brunt–Väisälä frequency and ambient wind of the  $i$ th layer.

In our simulations, the nonlinear interaction between the dynamics and microphysics produces a two-layer structure on the downwind of the mountain. The lower desaturated layer goes from the surface to  $z \approx 4$  km (Figs. 10c,f,i); the dry Brunt–Väisälä frequency in this layer  $N_l \approx 1.2 \times 10^{-2}$  s $^{-1}$ . The upper layer goes from  $z \approx 4$  km to the top of the troposphere, and its

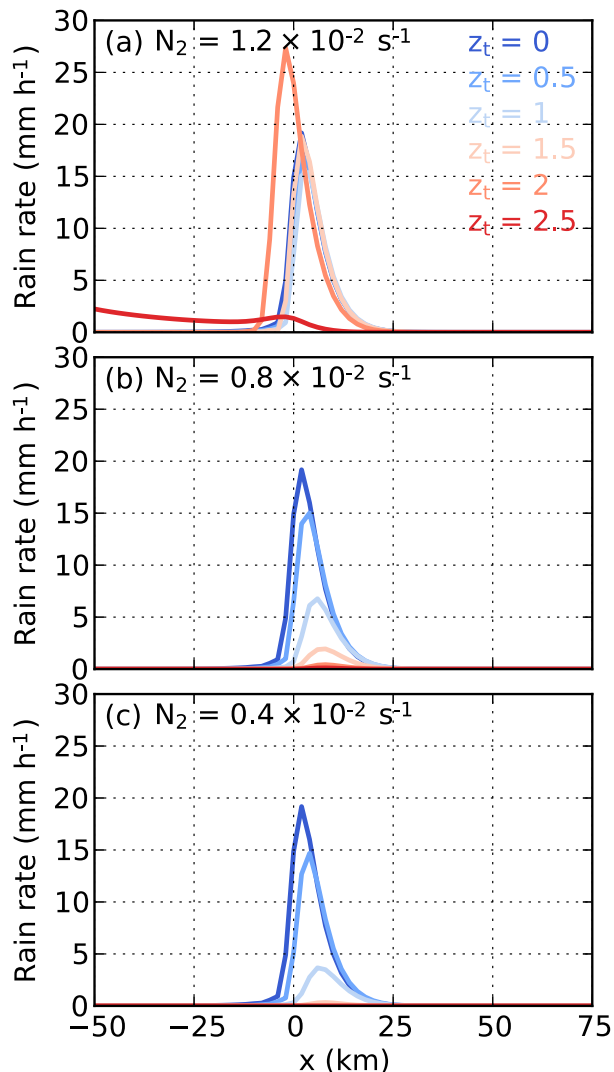


FIG. 9. As in Fig. 5, but for the liquid-only simulations with  $h_m = 1.5$  km and  $U = 20$  m s $^{-1}$ .

Brunt–Väisälä frequency is the moist Brunt–Väisälä frequency  $N_u = \sqrt{3} \times 10^{-3}$  s $^{-1}$ . In addition, the ambient wind is 20 m s $^{-1}$  throughout the whole atmosphere. Calculation shows that (3) is satisfied, indicating that lee waves can occur in these simulations.

In these simulations, the vertical velocity is almost independent of  $z_t$  (Figs. 10a,d,g), similar to that found in Durran and Klemp (1982). In this situation, the updraft-width effect is negligible. However, the vapor-transport effect is still active, as revealed by the decreasing cloud water mixing ratio with  $z_t$  (cf. Figs. 10c,f,i). Thus, Fig. 11a shows that increasing  $z_t$  decreases the rain rate. For smaller values of  $N_2$ , that is,  $0.8 \times 10^{-2}$  and  $0.4 \times 10^{-2}$  s $^{-1}$ , (3) is still satisfied and these simulations also produce lee waves. Increasing  $z_t$  therefore decreases the rain rate (Figs. 11b,c). In all the simulations with

$h_m = 0.7$  km,  $U = 20$  m s $^{-1}$ , the flow is not blocked (e.g., Figs. 10b,e,h).

## 5. Surface precipitation of mixed-phase simulations

In this section, we present the mixed-phase simulations to show the effect of ice-phase microphysics on the dynamics and precipitation. For each combination of  $h_m$  and  $U$ , only the simulation with  $z_t = 0$  km is shown in detail. Note that the simulation with  $z_t = 0$  km is independent of  $N_2$ . For the simulations with  $z_t > 0$  km, only the rain-rate distributions are presented; the details of the simulations are not presented because they are similar to those in the liquid-only simulations.

### a. $h_m = 0.7$ km and $U = 10$ m s $^{-1}$

Figure 12a shows the vertical velocity of the mixed-phase simulation with  $h_m = 0.7$  km,  $U = 10$  m s $^{-1}$ , and  $z_t = 0$  km. It can be seen that the updraft over the upwind slope is shallower in the mixed-phase simulation than in the liquid-only simulation (cf. Figs. 12a and 3a). In the mixed-phase simulations, as mentioned in section 2, the initial profile above the freezing level is subsaturated with respect to water. In this situation,  $N$  above the freezing level becomes larger. According to linear theory, the vertical wavelength is inversely proportional to  $N$  (Lin 2007, 109–112). Therefore, the vertical wavelength is shorter in the mixed-phase simulation than in the liquid-only simulation. Figure 12a also shows that the updraft over the upwind slope is mostly below the freezing level ( $\sim 3$  km). Figure 12b thus suggests that ice formation is negligible on the upwind side of the mountain. In addition, a shallower updraft leads to less condensation (cf. Figs. 12b and 3c), so Fig. 13a shows that the rain rate in the mixed-phase simulation is weaker than that in the liquid-only simulation (cf. Fig. 5a).

Figure 12b also shows that the inclusion of ice-phase microphysics produces surface precipitation between  $x = 25$  and 50 km, where no surface precipitation forms in the corresponding liquid-only simulation (cf. Fig. 3c). In the mixed-phase simulation, Fig. 12a reveals a strong updraft between  $z = 3$  and 10 km. This updraft leads to the formation of ice crystals (Fig. 12b), which grow and are subsequently converted to snow particles. Because the fall speeds of snow particles are relatively small, they are transported downwind as they fall. When the snow particles fall below the freezing level, they melt and produce surface precipitation at 25–50 km downwind of the mountain peak (Fig. 13a).

Figure 13a shows the rain-rate distributions of the mixed-phase simulations with  $h_m = 0.7$  km,  $U = 10$  m s $^{-1}$ ,

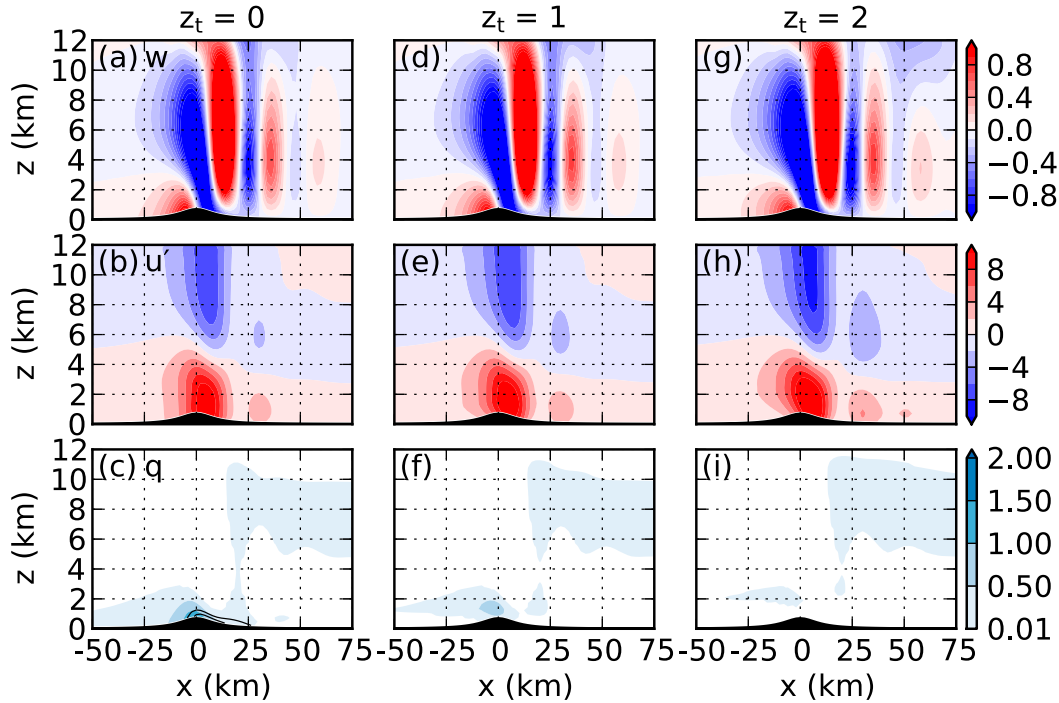


FIG. 10. Results at  $t = 20$  h of three liquid-only simulations with  $h_m = 0.7$  km,  $U = 20$  m s<sup>-1</sup>, and  $N_2 = 1.2 \times 10^{-2}$  s<sup>-1</sup>; values of  $z_t$  (km) are shown above each column. Rows show (a),(d),(g) the vertical velocity (m s<sup>-1</sup>); (b),(e),(h) the perturbation cross-mountain wind (m s<sup>-1</sup>); and (c),(f),(i) the cloud water mixing ratio (g kg<sup>-1</sup>; shaded) and rainwater mixing ratio (g kg<sup>-1</sup>; black contours starting from 0.001 g kg<sup>-1</sup> with a contour interval of 0.001 g kg<sup>-1</sup>).

and  $N_2 = 1.2 \times 10^{-2}$  s<sup>-1</sup>. When  $z_t$  increases from 0 to 0.5 km, the updraft also becomes slightly wider, similar to the liquid-only simulations. However, because the stable layer above the freezing level reduces the depth of the updraft, the updraft-width effect in the mixed-phase simulation is weaker than that in the liquid-only simulation. The updraft-width effect nearly counteracts the vapor-transport effect. Figure 13a therefore indicates that the rain rate in the simulation with  $z_t = 0.5$  km is similar to that in the simulation with  $z_t = 0$  km. As  $z_t$  further increases to 1 km, the updraft becomes even wider. Nevertheless, the updraft-width effect is substantially reduced by the stable layer above the freezing level, and becomes weaker than the vapor-transport effect. The rain rate in the simulation with  $z_t = 1$  km is therefore smaller than that in the simulation with  $z_t = 0.5$  km. In the simulations with  $z_t \geq 1.5$  km, the decelerated region moves upwind, as in the liquid-only simulations. Therefore, Fig. 13a shows that the rain rate near the mountain peak is very small. On the downwind side of the mountain, Fig. 13a reveals relatively large rain rates in the simulations with  $z_t \geq 1.5$  km. In these simulations, a strong updraft forms below  $z = 4$  km on the downwind side of the mountain. When the snow particles and rain droplets

fall through this updraft, they grow and consequently produce a relatively large rain rate. It is worth mentioning that the updraft below  $z = 4$  km is slowly moving downwind.

For a smaller  $N_2 = 0.8 \times 10^{-2}$  s<sup>-1</sup>, the updraft-width effects are generally weaker. In the simulations with  $z_t \leq 1.5$  km, the updraft-width effect is weaker than the vapor-transport effect. Figure 13b thus indicates that the rain rate decreases with  $z_t$ . In the simulations with  $z_t \geq 2$  km, the decelerated region moves upwind. Thus, no surface precipitation forms near the mountain peak. Nevertheless, the updraft aloft leads to the formation of ice crystals and consequently produces surface precipitation on the downwind side of the mountain (Fig. 13b). In the simulations with an even smaller  $N_2 = 0.4 \times 10^{-2}$  s<sup>-1</sup>, the updraft-width effects are even weaker. Figure 13c shows that increasing  $z_t$  simply decreases surface precipitation. In all simulations with  $N_2 = 0.4 \times 10^{-2}$  s<sup>-1</sup>, the decelerated regions do not move upwind.

b.  $h_m = 1.5$  km and  $U = 10$  m s<sup>-1</sup>

Figure 12c shows the vertical velocity of the mixed-phase simulation with  $h_m = 1.5$  km,  $U = 10$  m s<sup>-1</sup>, and  $z_t = 0$  km. In this simulation, the higher mountain

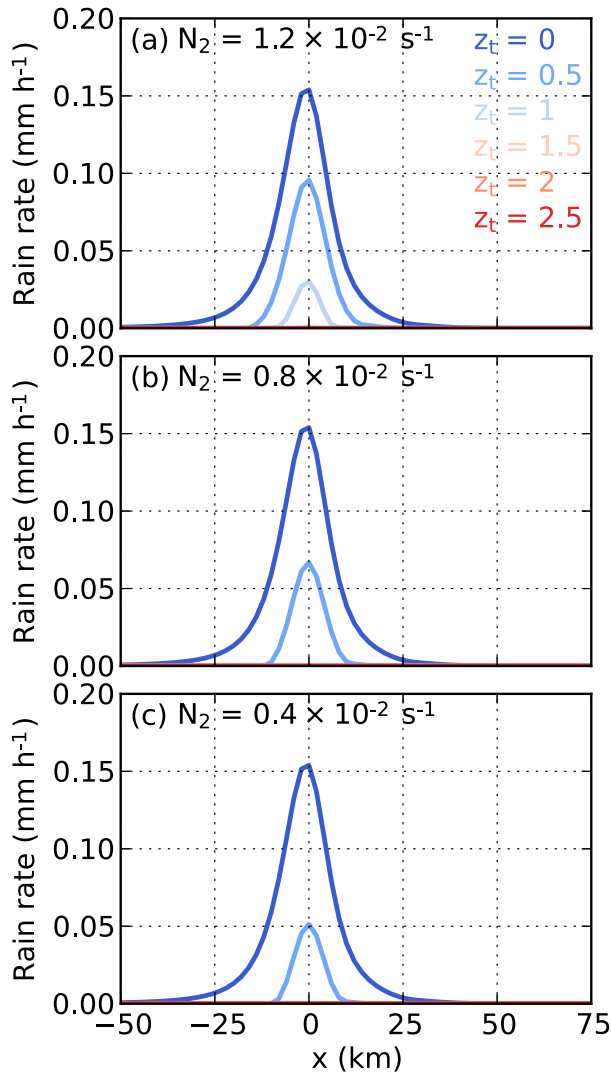


FIG. 11. As in Fig. 5, but for the liquid-only simulations with  $h_m = 0.7$  km and  $U = 20$  m s $^{-1}$ .

exerts a stronger orographic forcing, which overcomes the effect of the stable layer above the freezing level. The vertical velocity in the mixed-phase simulation is hence almost the same as that in the liquid-only simulation (cf. Fig. 6a). Figure 12c suggests that the updraft over the upwind slope extends above the freezing level, resulting in the formation of ice crystals (the ice water mixing ratio is so low that it does not appear in Fig. 12d). These ice crystals quickly grow and become snow particles (Fig. 12d), the melting of which consequently produces rainwater. In this mixed-phase simulation, the formation of precipitation is accelerated due to the presence of ice-phase microphysics. The mixed-phase simulation thus needs a shorter time to produce precipitation. For the simulations with  $z_t = 0$  km, Fig. 14a shows that the surface

precipitation occurs farther upwind in the mixed-phase simulation than in the liquid-only simulation (cf. Fig. 7a). On the downwind side of the mountain, Fig. 12c also reveals a strong updraft aloft. Ice crystals therefore form, leading to the formation of snow particles. These snow particles are also transported downwind as they fall. Therefore, they melt and produce rain droplets at 25–50 km downwind of the mountain peak (Fig. 12d). In addition, most of the rainwater is evaporated before the rain droplets fall to the surface. Thus, Fig. 14a shows that the rain rate is small on the downwind side of the mountain.

Figure 14a shows the effect of varying  $z_t$  on rain-rate distributions of the simulations with  $h_m = 1.5$  km,  $U = 10$  m s $^{-1}$ , and  $N_2 = 1.2 \times 10^{-2}$  s $^{-1}$ . The rain rates in the simulation with  $z_t = 0$  and 0.5 km are similar, as in the liquid-only simulations. However, unlike the liquid-only simulations, where the decelerated region moves upwind when  $z_t \geq 1.5$  km; in the mixed-phase simulations, the decelerated region moves upwind when  $z_t \geq 1$  km. Figure 14a thus indicates that the rain rate near the mountain is much smaller in the simulations with  $z_t \geq 1$  km than in the simulations with  $z_t < 1$  km. In the simulations with  $N_2 = 0.8 \times 10^{-2}$  s $^{-1}$ , Fig. 14b shows that the rain rate does not change as  $z_t$  increases from 0 to 0.5 km, and decreases as  $z_t$  further increases to 1 km, similar to the liquid-only simulations. In the liquid-only simulations, the decelerated region moves upwind only when  $z_t = 2.5$  km; while in the mixed-phase simulations, the decelerated region moves upwind when  $z_t \geq 1.5$  km. Figure 14b thus indicates that the rain rate becomes much smaller when  $z_t \geq 1.5$  km. In the simulations with  $N_2 = 0.4 \times 10^{-2}$  s $^{-1}$ , Fig. 14c reveals that the rain rate decreases with  $z_t$ , similar to the liquid-only simulations (cf. Fig. 7c). In all the mixed-phase simulations with  $h_m = 1.5$  km and  $U = 10$  m s $^{-1}$ , Fig. 14 indicates that the rain rates are small on the downwind side of the mountain.

*c.  $h_m = 1.5$  km and  $U = 20$  m s $^{-1}$*

Figure 12e shows the vertical velocity of the mixed-phase simulation with  $h_m = 1.5$  km,  $U = 20$  m s $^{-1}$ , and  $z_t = 0$  km. It can be seen that the updraft over the upwind slope is much shallower than that in the liquid-only simulation (cf. Fig. 8a). Figure 12f reveals that ice-phase microphysics is active in this simulation. As mentioned before, the presence of ice crystals accelerates the formation of precipitation. For the simulations with  $z_t = 0$  km, Fig. 15a shows that precipitation occurs farther upwind in the mixed-phase simulation than in the liquid-only simulation (cf. Fig. 9a). The precipitation efficiently removes moisture.

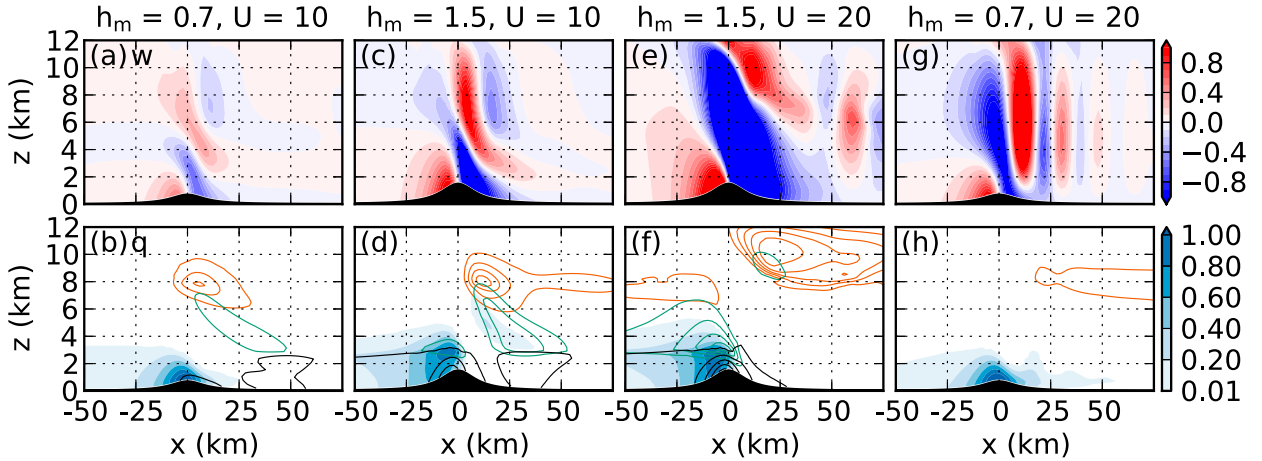


FIG. 12. Results at  $t = 20$  h of the mixed-phase simulations with  $z_t = 0$  km; values of  $h_m$  (km) and  $U$  ( $\text{m s}^{-1}$ ) are shown above each column. Rows show (a),(c),(e),(g) the vertical velocities ( $\text{m s}^{-1}$ ) and (b),(d),(f),(h) the cloud water mixing ratios ( $\text{g kg}^{-1}$ ; shaded), rain-water mixing ratios ( $\text{g kg}^{-1}$ ; black contours starting from  $0.01 \text{ g kg}^{-1}$  with a contour interval of  $0.02 \text{ g kg}^{-1}$ ), ice water mixing ratios ( $\text{g kg}^{-1}$ ; orange contours starting from  $0.01 \text{ g kg}^{-1}$  with a contour interval of  $0.02 \text{ g kg}^{-1}$ ), and snow water mixing ratios ( $\text{g kg}^{-1}$ ; green contours starting from  $0.05 \text{ g kg}^{-1}$  with a contour interval of  $0.1 \text{ g kg}^{-1}$ ). Graupel water mixing ratio is negligible in these simulations and is therefore not shown.

The upwind atmosphere becomes drier, and hence has a larger  $N$ . According to linear theory, the vertical wavelength is inversely proportional to  $N$  (Lin 2007, 109–112). Therefore, Fig. 12e indicates that the updraft over the upwind slope in the mixed-phase simulation is shallower than that in the liquid-only simulation.

Figure 15 shows the rain-rate distributions of all the simulations with  $h_m = 1.5$  km and  $U = 20 \text{ m s}^{-1}$ . Comparing with Fig. 9, it is found that the response of rain rate to both  $N_2$  and  $z_t$  in the mixed-phase simulations is similar to that in the liquid-only simulations, except that the surface precipitation occurs farther upwind in the mixed-phase simulations.

#### d. $h_m = 0.7$ km and $U = 20 \text{ m s}^{-1}$

Figure 12g shows that lee waves also occur in the mixed-phase simulations with  $h_m = 0.7$  km,  $U = 20 \text{ m s}^{-1}$ , and  $z_t = 0$  km. Actually, lee waves occur in all the mixed-phase simulations with  $h_m = 0.7$  km and  $U = 20 \text{ m s}^{-1}$ . Because the updraft over the upwind slope are mostly below the freezing level, Fig. 12h shows that ice crystals hardly form in the nominally mixed-phase simulations. Therefore, Fig. 16 shows that the rain rate in the mixed-phase simulations is almost the same as that in the liquid-only simulations (cf. Fig. 11).

## 6. Upwind movement of the decelerated region

As has been shown, when  $z_t$  is greater than a certain value, the near surface decelerated region on the

upwind side moves upwind. This upwind movement can be understood with linear theory. Following Baines (1995, 175–176), we consider a layer going from  $z = 0$  to  $z_t$ , with a rigid bottom boundary condition and a pliant upper boundary condition. The group velocity of the wave propagating in this layer is

$$c_g = U \pm \frac{N_2 m^2}{(k^2 + m^2)^{3/2}}, \quad (5)$$

where  $k$  and  $m$  are, respectively, the horizontal and vertical wavenumber. Note that  $N_2$  is the Brunt–Väisälä frequency of the considered layer. Here, we consider the longest wave, which is the fastest wave, so  $k$  goes to 0. For the longest wave, the vertical wavenumber is

$$m = \left(j + \frac{1}{2}\right) \frac{\pi}{z_t}, \quad j = 0, 1, 2, \dots \quad (6)$$

When  $k = 0$ , (5) indicates that the fastest wave corresponds to  $j = 0$ . The group velocity is therefore

$$c_g = U - \frac{2N_2 z_t}{\pi}. \quad (7)$$

Note that the minus sign is taken in (7) because we are concerned with the upwind propagating wave. By setting the rhs of (7) to 0, we find that the upwind movement of the decelerated region is controlled by a nondimensional parameter  $N_2 z_t / U$  and its critical value is  $\pi/2$ , which is approximately 1.6. When  $N_2 z_t / U > 1.6$ , the decelerated region moves upwind;

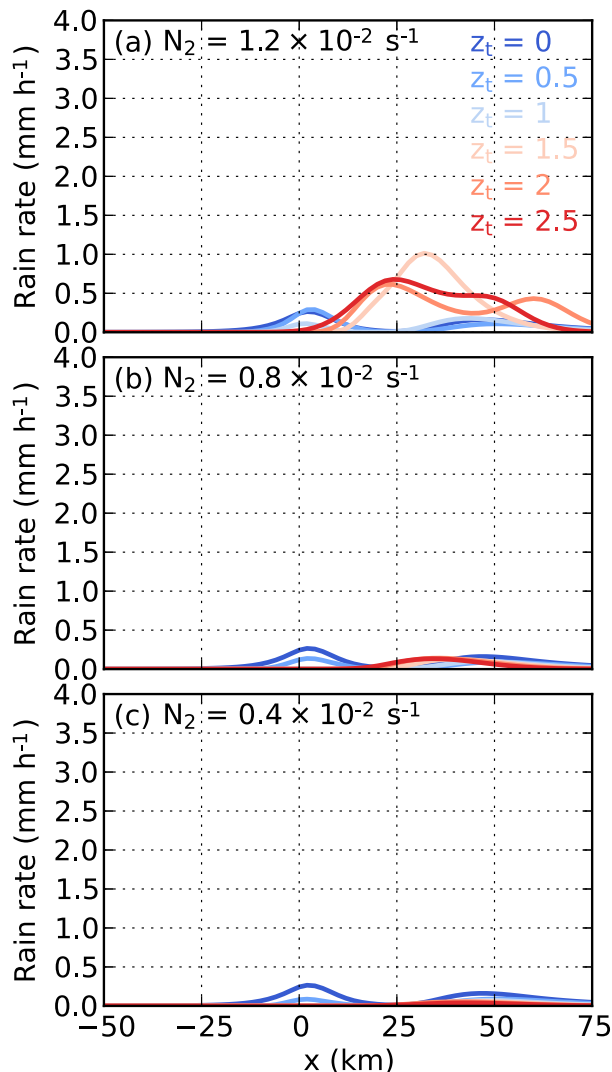


FIG. 13. As in Fig. 5, but for the mixed-phase simulations with  $h_m = 0.7$  km and  $U = 10$  m s $^{-1}$ .

when  $N_2 z_t / U < 1.6$ , the decelerated region stays near the mountain peak.

Table 2 shows that the decelerated region moves upwind in 5 out of the 12 simulated combinations of  $h_m$ ,  $U$ , and  $N_2$  (Table 1). In addition, the upwind movement occurs in these 5 combinations no matter whether ice-phase microphysics is included or not. We define the smallest  $z_t$  with which the simulated decelerated region moves upwind as  $z_{t,c}$ . Table 2 lists the values of  $z_{t,c}$  and the corresponding values of  $N_2 z_{t,c} / U$  for the 5 combinations. For the liquid-only simulations, the simulated critical values are generally close to the theoretical value. For the mixed-phase simulations, the simulated critical values are close to the theoretical values except for the two combinations with  $h_m = 1.5$  km and  $U = 10$  m s $^{-1}$  due to more complex microphysical effects on the effective stability.

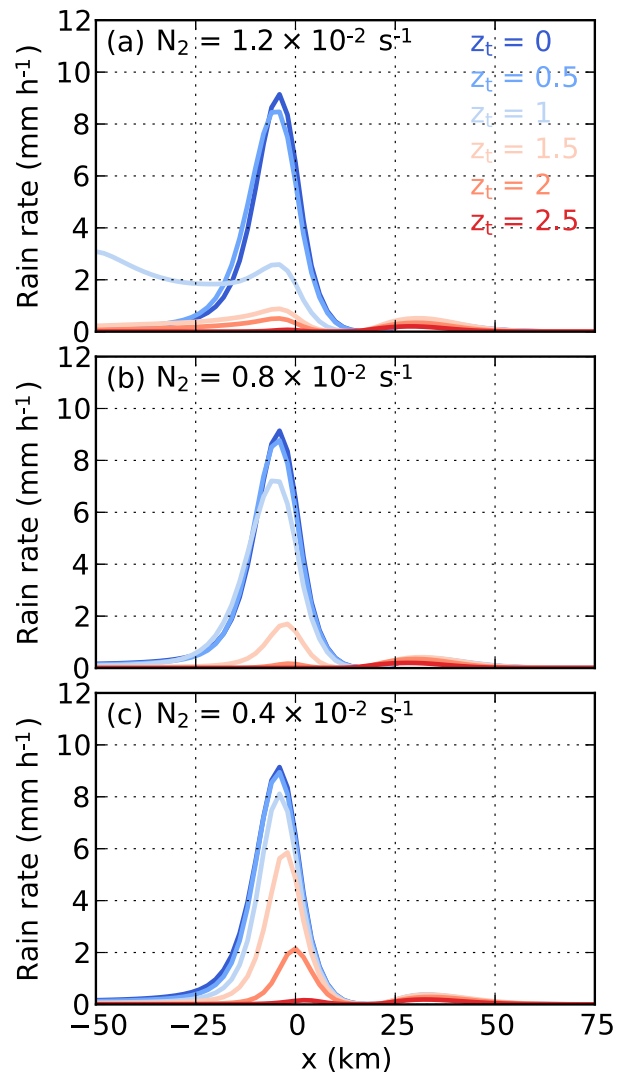


FIG. 14. As in Fig. 5, but for the mixed-phase simulations with  $h_m = 1.5$  km and  $U = 10$  m s $^{-1}$ .

## 7. Summary

Nearly moist-neutral flows are frequently observed in orographic precipitation events. Previous studies of nearly moist-neutral flow either assumed the whole atmosphere to be saturated or assumed a constant relative humidity. However, there are times when we observe subsaturated, low-level layers below the saturated, nearly moist-neutral, upper-level layers. In this study, a series of idealized 2D simulations are performed to study the response of orographic precipitation to the Brunt-Väisälä frequency  $N_2$ , and depth  $z_t$  of the subsaturated low-level layers. The effects of cross-mountain wind speed  $U$  and cloud microphysics are also investigated.

The response of orographic precipitation is partially controlled by a nondimensional parameter  $N_2 z_t / U$ .

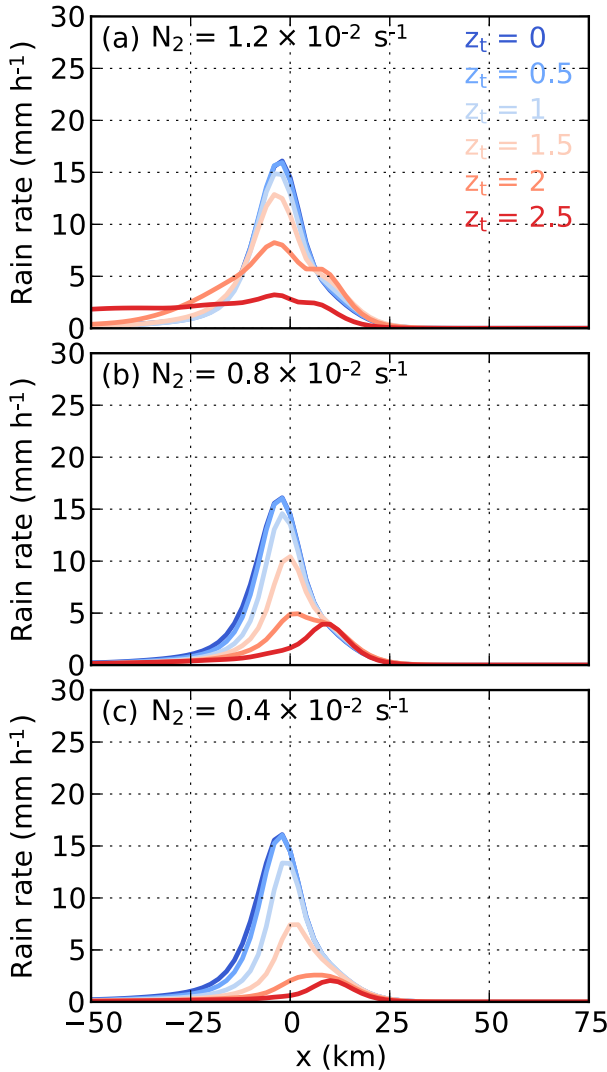


FIG. 15. As in Fig. 5, but for the mixed-phase simulations with  $h_m = 1.5$  km and  $U = 20$  m s $^{-1}$ .

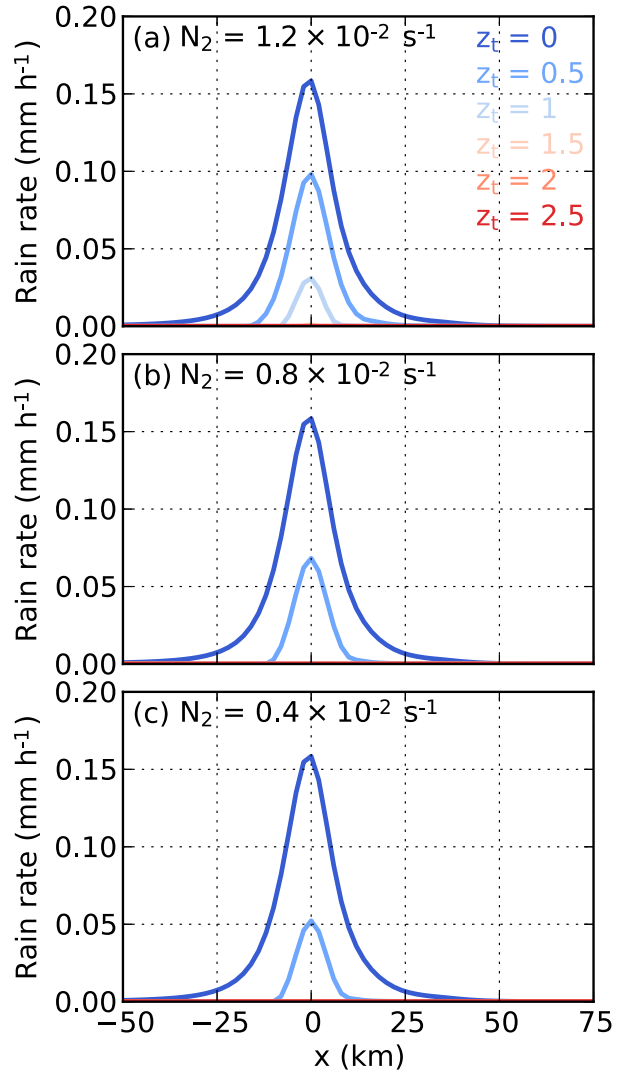


FIG. 16. As in Fig. 5, but for the mixed-phase simulations with  $h_m = 0.7$  km and  $U = 20$  m s $^{-1}$ .

When  $N_2 z_t / U$  exceeds a critical value, the decelerated region on the upwind slope of the mountain moves upwind, leading to a shallow and weak updraft near the mountain peak. The surface precipitation therefore becomes very weak near the mountain peak. The critical values of  $N_2 z_t / U$  determined from the simulations are close to that derived from linear theory (i.e., 1.6).

When  $N_2 z_t / U$  is smaller than the critical value, increasing  $z_t$  has two competing effects. On the one hand, increasing  $z_t$  decreases the amount of vapor transported to the mountain, and tends to decrease surface precipitation. This effect is the vapor-transport effect. On the other hand, increasing  $z_t$  enhances flow blocking. This increases the width of the updraft on the upwind side of the mountain, and tends to increase surface precipitation. This effect is the updraft-width effect.

When the vapor-transport effect dominates, surface precipitation decreases with  $z_t$ . When the updraft-width effect dominates, surface precipitation increases with  $z_t$ .

When  $N_2$ ,  $z_t$ , and the microphysics scheme are fixed, increasing the maximum mountain height  $h_m$  or  $U$  generally increases the surface precipitation. However, when  $h_m = 0.7$  km and  $U = 20$  m s $^{-1}$ , the simulations produce lee waves, which substantially reduces the surface precipitation. In addition, due to the difference in initial profiles and the inclusion of ice-phase microphysics, the surface precipitations in the mixed-phase simulations are generally different from those in the liquid-only simulations. Nevertheless, in the mixed-phase simulations, the response of surface precipitation to subsaturated low-level layers is similar to that in the liquid-only simulations.

TABLE 2. Simulated critical values of  $N_2 z_{t,c}/U$ . Only the combinations of  $h_m$ ,  $U$ , and  $N_2$  that produce an upwind movement of decelerated region are shown. The values outside the parentheses are for the liquid-only simulations while those in the parentheses are for the mixed-phase simulations.

Combination	$z_{t,c}$ (km)	$N_2 z_{t,c}/U$
$h_m = 0.7$ km, $U = 10$ m s <sup>-1</sup> , $N_2 = 1.2 \times 10^{-2}$ s <sup>-1</sup>	1.5 (1.5)	1.8 (1.8)
$h_m = 0.7$ km, $U = 10$ m s <sup>-1</sup> , $N_2 = 0.8 \times 10^{-2}$ s <sup>-1</sup>	2 (2)	1.6 (1.6)
$h_m = 1.5$ km, $U = 10$ m s <sup>-1</sup> , $N_2 = 1.2 \times 10^{-2}$ s <sup>-1</sup>	1.5 (1)	1.8 (1.2)
$h_m = 1.5$ km, $U = 10$ m s <sup>-1</sup> , $N_2 = 0.8 \times 10^{-2}$ s <sup>-1</sup>	2.5 (1.5)	2.0 (1.2)
$h_m = 1.5$ km, $U = 20$ m s <sup>-1</sup> , $N_2 = 1.2 \times 10^{-2}$ s <sup>-1</sup>	2.5 (2.5)	1.5 (1.5)

**Acknowledgments.** We thank Annareli Morales for helpful discussions. The soundings shown in Fig. 1 were downloaded from Wyoming Weather Web (<http://weather.uwyo.edu/upperair/sounding.html>). This study is supported by Chinese NSF Grant 41675134. The visit of S. Fu to NCAR is supported by China Scholarship Council. The National Center for Atmospheric Research is sponsored by the National Science Foundation.

#### REFERENCES

- Baines, P. G., 1995: *Topographic Effects in Stratified Flow*. Cambridge University Press, 482 pp.
- Berg, H. W. S., R. E. Stewart, and P. I. Joe, 2017: The characteristics of precipitation observed over Cypress Mountain during the SNOW-V10 campaign. *Atmos. Res.*, **197**, 356–369, <https://doi.org/10.1016/j.atmosres.2017.06.009>.
- Bougeault, P., and Coauthors, 2001: The MAP special observing period. *Bull. Amer. Meteor. Soc.*, **82**, 433–462, [https://doi.org/10.1175/1520-0477\(2001\)082<0433:TMSOP>2.3.CO;2](https://doi.org/10.1175/1520-0477(2001)082<0433:TMSOP>2.3.CO;2).
- Colle, B. A., 2004: Sensitivity of orographic precipitation to changing ambient conditions and terrain geometries: An idealized modeling perspective. *J. Atmos. Sci.*, **61**, 588–606, [https://doi.org/10.1175/1520-0469\(2004\)061<0588:SOOPTC>2.0.CO;2](https://doi.org/10.1175/1520-0469(2004)061<0588:SOOPTC>2.0.CO;2).
- , and C. F. Mass, 2000: The 5–9 February 1996 flooding event over the Pacific Northwest: Sensitivity studies and evaluation of the MM5 precipitation forecasts. *Mon. Wea. Rev.*, **128**, 593–617, [https://doi.org/10.1175/1520-0493\(2000\)128<0593:TFFEOT>2.0.CO;2](https://doi.org/10.1175/1520-0493(2000)128<0593:TFFEOT>2.0.CO;2).
- , R. B. Smith, and D. A. Wesley, 2013: Theory, observations, and predictions of orographic precipitation. *Mountain Weather Research and Forecasting*, F. K. Chow, S. F. J. De Wekker, and B. J. Snyder, Eds., Springer, 291–344, [https://doi.org/10.1007/978-94-007-4098-3\\_6](https://doi.org/10.1007/978-94-007-4098-3_6).
- Dettinger, M. D., F. M. Ralph, T. Das, P. J. Neiman, and D. R. Cayan, 2011: Atmospheric rivers, floods and the water resources of California. *Water*, **3**, 445–478, <https://doi.org/10.3390/w3020445>.
- Doswell, C. A., C. Ramis, R. Romero, and S. Alonso, 1998: A diagnostic study of three heavy precipitation episodes in the western Mediterranean Region. *Wea. Forecasting*, **13**, 102–124, [https://doi.org/10.1175/1520-0434\(1998\)013<0102:ADSOTH>2.0.CO;2](https://doi.org/10.1175/1520-0434(1998)013<0102:ADSOTH>2.0.CO;2).
- Durran, D. R., and J. B. Klemp, 1982: The effects of moisture on trapped mountain lee waves. *J. Atmos. Sci.*, **39**, 2490–2506, [https://doi.org/10.1175/1520-0469\(1982\)039<2490:TEOMOT>2.0.CO;2](https://doi.org/10.1175/1520-0469(1982)039<2490:TEOMOT>2.0.CO;2).
- Flatau, P. J., R. L. Walko, and W. R. Cotton, 1992: Polynomial fits to saturation vapor pressure. *J. Appl. Meteor.*, **31**, 1507–1513, [https://doi.org/10.1175/1520-0450\(1992\)031<1507:PFTSVP>2.0.CO;2](https://doi.org/10.1175/1520-0450(1992)031<1507:PFTSVP>2.0.CO;2).
- Galewsky, J., and A. Sobel, 2005: Moist dynamics and orographic precipitation in Northern and central California during the New Year's Flood of 1997. *Mon. Wea. Rev.*, **133**, 1594–1612, <https://doi.org/10.1175/MWR2943.1>.
- Ge, X., T. Li, S. Zhang, and M. Peng, 2010: What causes the extremely heavy rainfall in Taiwan during Typhoon Morakot (2009)? *Atmos. Sci. Lett.*, **11**, 46–50, <https://doi.org/10.1002/asl.255>.
- Houze, R. A., Jr., 2012: Orographic effects on precipitating clouds. *Rev. Geophys.*, **50**, RG1001, <https://doi.org/10.1029/2011RG000365>.
- Jiang, Q., 2003: Moist dynamics and orographic precipitation. *Tellus*, **55A**, 301–316, <https://doi.org/10.3402/tellus.v55i4.14577>.
- Kirshbaum, D. J., B. Adler, N. Kalthoff, C. Barthlott, and S. Serafin, 2018: Moist orographic convection: Physical mechanisms and links to surface-exchange processes. *Atmosphere*, **9**, 80, <https://doi.org/10.3390/atmos9030080>.
- Kuo, Y.-H., and G. T.-J. Chen, 1990: The Taiwan Area Mesoscale Experiment (TAMEX): An overview. *Bull. Amer. Meteor. Soc.*, **71**, 488–503, [https://doi.org/10.1175/1520-0477\(1990\)071<0488:TTAMEA>2.0.CO;2](https://doi.org/10.1175/1520-0477(1990)071<0488:TTAMEA>2.0.CO;2).
- Lehner, M., R. Rotunno, and C. D. Whiteman, 2016: Flow regimes over a basin induced by upstream katabatic flows—An idealized modeling study. *J. Atmos. Sci.*, **73**, 3821–3842, <https://doi.org/10.1175/JAS-D-16-0114.1>.
- Lin, Y.-L., 2007: *Mesoscale Dynamics*. Cambridge University Press, 630 pp.
- , D. B. Ensley, S. Chiao, and C.-Y. Huang, 2002: Orographic influences on rainfall and track deflection associated with the passage of a tropical cyclone. *Mon. Wea. Rev.*, **130**, 2929–2950, [https://doi.org/10.1175/1520-0493\(2002\)130<2929:OIORAT>2.0.CO;2](https://doi.org/10.1175/1520-0493(2002)130<2929:OIORAT>2.0.CO;2).
- Markowski, P. M., and Y. P. Richardson, 2010: *Mesoscale Meteorology in Midlatitudes*. Wiley-Blackwell, 424 pp.
- Miglietta, M. M., and R. Rotunno, 2005: Simulations of moist nearly neutral flow over a ridge. *J. Atmos. Sci.*, **62**, 1410–1427, <https://doi.org/10.1175/JAS3410.1>.
- , and —, 2006: Further results on moist nearly neutral flow past a ridge. *J. Atmos. Sci.*, **63**, 2881–2897, <https://doi.org/10.1175/JAS3793.1>.
- , and —, 2009: Numerical simulations of conditionally unstable flows over a mountain ridge. *J. Atmos. Sci.*, **66**, 1865–1885, <https://doi.org/10.1175/2009JAS2902.1>.
- , and —, 2014: Numerical simulations of sheared conditionally unstable flows over a mountain ridge. *J. Atmos. Sci.*, **71**, 1747–1762, <https://doi.org/10.1175/JAS-D-13-0297.1>.
- Morales, A., H. Morrison, and D. J. Posselt, 2018: Orographic precipitation response to microphysical parameter perturbations for idealized moist nearly neutral flow. *J. Atmos. Sci.*, **75**, 1933–1953, <https://doi.org/10.1175/JAS-D-17-0389.1>.
- Morrison, H., J. A. Curry, and V. I. Khvorostyanov, 2005: A new double-moment microphysics parameterization for application in cloud and climate models. Part I: Description.

- J. Atmos. Sci.*, **62**, 1665–1677, <https://doi.org/10.1175/JAS3446.1>.
- , G. Thompson, and V. Tatarskii, 2009: Impact of cloud microphysics on the development of trailing stratiform precipitation in a simulated squall line: Comparison of one- and two-moment schemes. *Mon. Wea. Rev.*, **137**, 991–1007, <https://doi.org/10.1175/2008MWR2556.1>.
- Peterson, T. C., L. O. Grant, W. R. Cotton, and D. C. Rogers, 1991: The effect of decoupled low-level flow on winter orographic clouds and precipitation in the Yampa River valley. *J. Appl. Meteor.*, **30**, 368–386, [https://doi.org/10.1175/1520-0450\(1991\)030<0368:TEODLL>2.0.CO;2](https://doi.org/10.1175/1520-0450(1991)030<0368:TEODLL>2.0.CO;2).
- Ralph, F. M., P. J. Neiman, and R. Rotunno, 2005: Dropsonde observations in low-level jets over the northeastern Pacific Ocean from CALJET-1998 and PACJET-2001: Mean vertical-profile and atmospheric-river characteristics. *Mon. Wea. Rev.*, **133**, 889–910, <https://doi.org/10.1175/MWR2896.1>.
- , —, G. A. Wick, S. I. Gutman, M. D. Dettinger, D. R. Cayan, and A. B. White, 2006: Flooding on California's Russian River: Role of atmospheric rivers. *Geophys. Res. Lett.*, **33**, L13801, <https://doi.org/10.1029/2006GL026689>.
- , T. Coleman, P. J. Neiman, R. J. Zamora, and M. D. Dettinger, 2013: Observed impacts of duration and seasonality of atmospheric-river landfalls on soil moisture and runoff in coastal Northern California. *J. Hydrometeor.*, **14**, 443–459, <https://doi.org/10.1175/JHM-D-12-076.1>.
- Rotunno, R., and R. Ferretti, 2001: Mechanisms of intense Alpine rainfall. *J. Atmos. Sci.*, **58**, 1732–1749, [https://doi.org/10.1175/1520-0469\(2001\)058<1732:MOIAR>2.0.CO;2](https://doi.org/10.1175/1520-0469(2001)058<1732:MOIAR>2.0.CO;2).
- , and R. A. Houze, 2007: Lessons on orographic precipitation from the Mesoscale Alpine Programme. *Quart. J. Roy. Meteor. Soc.*, **133**, 811–830, <https://doi.org/10.1002/qj.67>.
- Sawyer, J. S., 1956: The physical and dynamical problems of orographic rain. *Weather*, **11**, 375–381, <https://doi.org/10.1002/j.1477-8696.1956.tb00264.x>.
- Scorer, R. S., 1949: Theory of waves in the lee of mountains. *Quart. J. Roy. Meteor. Soc.*, **75**, 41–56, <https://doi.org/10.1002/qj.49707532308>.
- Skamarock, W. C., and Coauthors, 2008: A description of the Advanced Research WRF version 3. NCAR Tech. Note NCAR/TN-475+STR, 113 pp., <https://doi.org/10.5065/D68S4MVH>.
- Stoelinga, M. T., R. E. Stewart, G. Thompson, and J. M. Thériault, 2013: Microphysical processes within winter orographic cloud and precipitation systems. *Mountain Weather Research and Forecasting*, F. K. Chow, S. F. J. De Wekker, and B. J. Snyder, Eds., Springer, 291–344, [https://doi.org/10.1007/978-94-007-4098-3\\_7](https://doi.org/10.1007/978-94-007-4098-3_7).
- Tushaus, S. A., D. J. Posselt, M. M. Miglietta, R. Rotunno, and L. Delle Monache, 2015: Bayesian exploration of multivariate orographic precipitation sensitivity for moist stable and neutral flows. *Mon. Wea. Rev.*, **143**, 4459–4475, <https://doi.org/10.1175/MWR-D-15-0036.1>.
- Xue, L., A. Teller, R. Rasmussen, I. Geresdi, and Z. Pan, 2010: Effects of aerosol solubility and regeneration on warm-phase orographic clouds and precipitation simulated by a detailed bin microphysical scheme. *J. Atmos. Sci.*, **67**, 3336–3354, <https://doi.org/10.1175/2010JAS3511.1>.